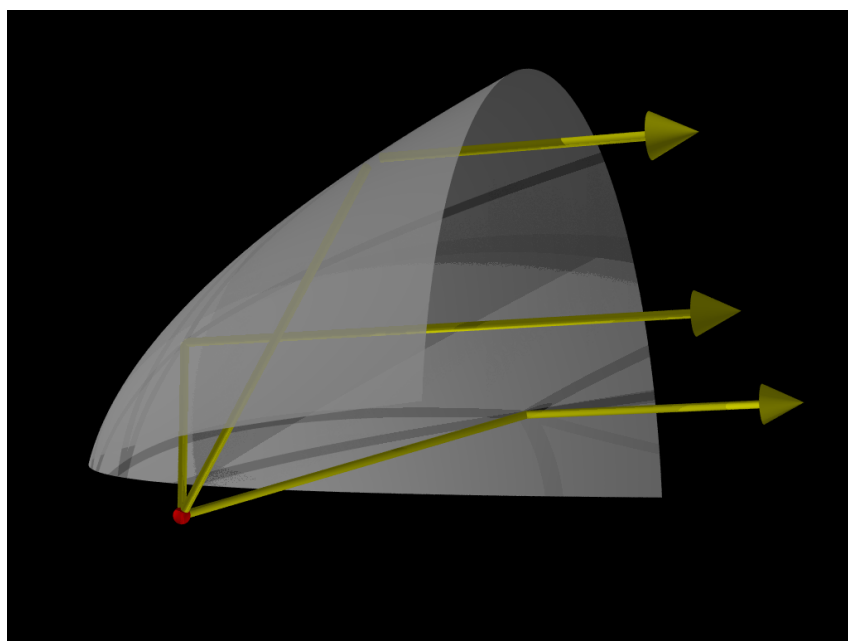# Angle-Resolved Cathodoluminescence Spectroscopy of Plasmonic Nanoantennas

Toon Coenen

Supervisors:
Drs. Ernst Jan Vesseur and Prof. Dr. Albert Polman

The cover shows an off axis paraboloid mirror collecting light emission from a point source located in its focal point, after which it is redirected sideways in a parallel beam of light.

Abstract

Surface plasmons are plasma oscillations on a metal-dielectric interface. Plasmons provide a means to shrink the wavelength of light and to confine it to nanoscale volumes. To directly probe plasmon behavior a technique with high spatial resolution is required.

In cathodoluminescence (CL) spectroscopy an electron beam is used as plasmon excitation source. In our experimental setup the electron beam of a scanning electron microscope (SEM) is used which has a beam spot with a diameter of 10 nm allowing high resolution spatially resolved CL-spectroscopy.

This is used to investigate the influence of focused-ion-beam (FIB) milling on the propagation of surface plasmon polaritons (SPPs) on single crystal gold. It is shown that the milling process does not have a significant influence on the SPP propagation length for visible frequencies. Also whispering gallery modes in annular and elliptical groove resonators and Fabry-Pérot modes in a silver wedge are studied using this technique.

In this thesis a novel way to measure the CL emission pattern is presented. By combining this technique with the point like electron beam excitation it is possible to study the influence of plasmonic structures on the emission pattern of a point source which possibly could provide a better understanding of the interaction of single emitters with plasmonic antennas.

We apply this technique to a single crystal gold ridge and a metal nanoparticle array antenna to obtain the emission pattern as function of excitation position. We show that the emission pattern strongly depends on excitation position.

Contents

Chapter 1

Introduction

1.1 Introduction

Surface Plasmons are collective electron oscillations on a metal-dielectric interface. These oscillations are damped exponentially in the direction normal to the surface but they can propagate as transverse magnetic waves along a metal surface with the speed of light. These propagating plasma oscillations are called surface plasmon polaritons (SPPs). Last decades the field of plasmonics has gained enormous interest. The ability of plasmonic structures to shrink the wavelength of light and to confine it to extremely small volumes well below the diffraction limit is interesting for numerous potential applications in sensing, optoelectronics, metamaterials and photovoltaics [1–3].

Since many plasmonic systems are smaller than the diffraction limit of light it is impossible to use regular far-field optical microscopies to accurately probe these systems since their spatial resolutions are limited by Abbe's law of diffraction.

Near-field scanning optical microscopy (NSOM) is an optical technique of which the spatial resolution is only limited by the apex diameter of the tip (down to ∼50 nm). In order to probe plasmonic structures the near-field tip has to be within the evanescent field of the structure which means that it has to in close proximity of the sample surface. Consequently the metal-coated tip can influence the local photonic environment, thereby distorting experimental observations. Additionally, it is not possible in a free space experiment to excite SPPs on a metal surface with light directly due to a momentum mismatch between photon and plasmon. An incoupling structure like a grating or hole array is needed to provide the required momentum step.

An alternative way to study plasmonic structures is cathodoluminescence (CL) spectroscopy. In CL-spectroscopy a beam of electrons is used as an excitation source. In our experimental setup the tightly focused electron beam of a scanning electron microscope (SEM) acts as the electron source. The electrons have an energy of 30 keV which corresponds to a speed of approximately $c/3$. A 30 keV electron packs much more momentum than a visible photon and as a result its relativistic de Broglie wavelength of 7 pm is five orders of magnitude smaller than the wavelength of visible light. Additionally, the magnetic field of the electron diverges towards its trajectory so the interaction with the photonic environment is strongest at that point [5]. As a consequence the resolution of CL is roughly the electron beam diameter, which is about 10 nm in our SEM, giving it a much higher spatial resolution than optical techniques.
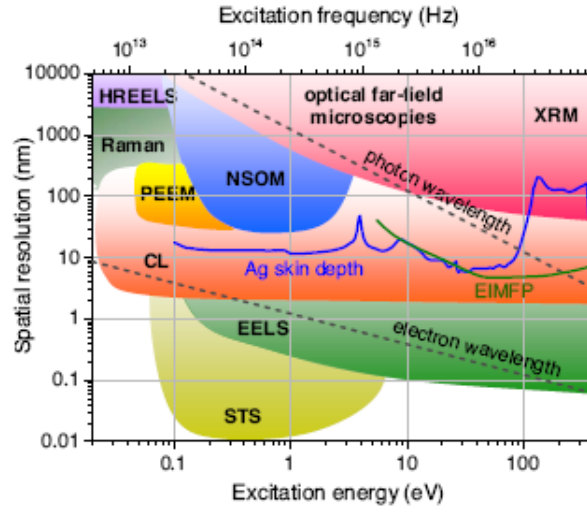
Figure 1.1: Spatial resolution as function of excitation energy for different optical and electron beam techniques [4].

In Fig. 1.1 the spatial resolution as function of excitation energy for different spatially resolved spectroscopy techniques is shown. For comparison, the photon wavelength, electron wavelength and the Ag-skin depth for these energies are also shown. CL-spectroscopy maintains a high resolution over a large energy range and is only superseded in terms of spatial resolution by scanning tunneling microscopy (STM) and scanning transmission electron microscopy (STEM) based techniques.

1.2 Electron beam excitation
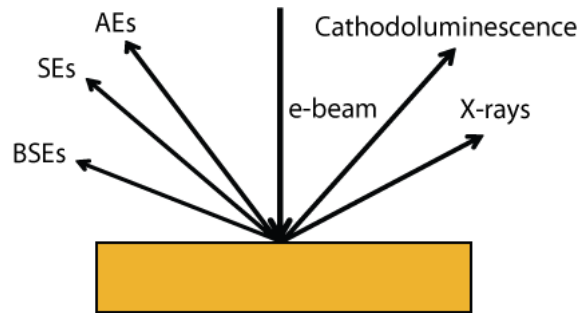
Figure 1.2: Different processes occurring upon e-beam excitation.

When the energetic electron beam hits a sample surface several processes can occur [4, 6] (Fig. 1.2). The electrons can scatter inelastically from the electron clouds of the atoms, producing low-energy secondary electrons (SEs) which can be used for imaging. The electrons can also scatter elastically from the nuclei producing high-energy backscattered electrons. The amount of the backscattered electrons (BSEs) depends on the atomic number Z, crystal structure and crystal orientation so BSE-imaging can be used to contrast areas with different atomic composition or crystallographic properties [7]. Furthermore, the energetic beam-

electrons can knock out core electrons resulting in the emission of Auger electrons(AEs) which can be used for Auger electron spectroscopy (AES) and x-rays which can be used for energy-dispersive x-ray (EDX) spectroscopy.

The fields of the electrons can excite atoms or ions into a higher quantum state which after radiative relaxation leads to cathodoluminescence. This relaxation process is very similar to photoluminescence although the excitation mechanism is quite different. Photons in general mostly couple to strong dipole modes. The coupling to other modes is limited by stringent selection rules. Electrons however, can efficiently excite non dipolar transitions because they can transfer relatively large momenta compared to photons [4]. The generation of luminescence is incoherent with respect to the field of the incoming electron. An incoherent luminesence spectrum of Ce(III):YAG which is a commercial phosphor, is shown in Fig. 1.3. Light generation by electrons is very efficient in this material ($\sim 10^3$ photons/e$^-$), which makes the CL-signal relatively intense and even visible to the naked eye.
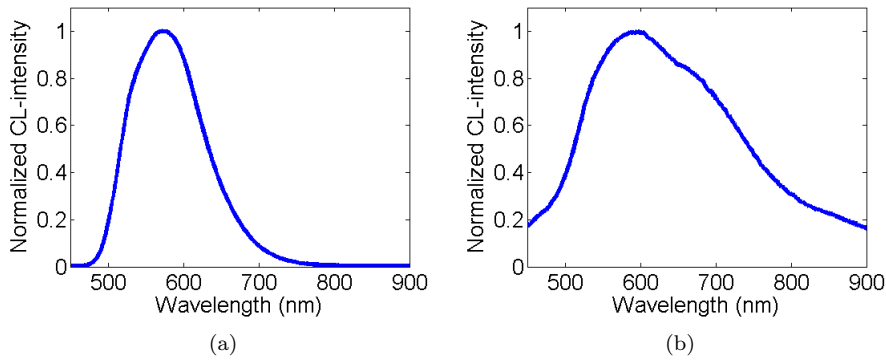
Figure 1.3: (a) Incoherent cathodoluminescence spectrum for Cerium(III) embedded in a YAG matrix (b) Coherent transition radiation spectrum for a single-crystalline gold surface. These spectra were not corrected for detection system response.

1.3 Theory of Electron Induced Radiation Emission

When the speed of the electron in a medium is higher than the phase velocity of light in that medium (v> c/$\sqrt{\varepsilon}$), the electron emits Cherenkov radiation. In this thesis we will neglect the process of Cherenkov radiation emission because its contribution to the CL-signal is negligible [8].

Radiative relaxation of electron-hole pairs in metals is not important because electronic relaxation channels are much faster. In CL-spectroscopy of metals, light emission is dominated by coherent interaction with the free electron plasma of the metal. When an electron moves through a dielectric-metal boundary the electron and its image charge induce a dipole moment normal to the surface. This dipole can either decay into SPPs or into far field photons (transition radiation (TR)). The SPPs can be coupled to the far-field through radiation losses in nanophotonic structures such as a grating or through surface roughness. An example of a TR-spectrum is shown in Fig. 1.3(b) for a single crystalline gold substrate. Theoretical calculations accurately describe the emission probability of TR as function of zenithal angle θ [4, 5]. Equation 1.1 describes the TR-emission probability per incoming

electron per unit bandwidth.

$$P_{TR}(\omega) = \frac{1}{\hbar k} \int_{-\pi/2}^{0} \sin(\theta) d\theta |\mathbf{f}(\theta, \omega)|^2 \tag{1.1}$$

To obtain $P_{TR}(\lambda)$ we have to include a normalization factor

$$P_{TR}(\lambda) = \frac{\omega^2}{2\pi c} \cdot P_{TR}(\omega) \tag{1.2}$$

$\mathbf{f}(\theta, \omega)$ describes the emission amplitude:

$$\mathbf{f}(\theta, \omega) = -\imath k D \mu_1 \cos(\theta) \hat{\phi} \tag{1.3}$$

The unit vector $\hat{\phi}$ can be explained by the fact that the emission of TR is azimuthally symmetric. $\mu_1 D$ represents the boundary coefficient for the air halfspace where

$$\mu_1 = \frac{1}{v} \left(\frac{\omega \varepsilon_2 + v q_{z2} \varepsilon_1}{q^2 - k^2 \varepsilon_1} - \frac{\omega \varepsilon_1 + v q_{z2} \varepsilon_1}{q^2 - k^2 \varepsilon_2} \right) \tag{1.4}$$

and

$$D = \frac{2\imath e q_{\parallel}/c}{q_{z1} \varepsilon_2 + q_{z2} \varepsilon_1} \tag{1.5}$$

In these equations ε_j represent the dielectric functions of the dielectric (1) and the metal (2) respectively, v is the electron velocity calculated from the electron energy and mass, $q_{\parallel} = k \sin(\theta)$, $q = \sqrt{q_{\parallel}^2 + (\omega/v)^2}$ and $q_{zj} = \sqrt{k^2 \varepsilon_j - q_{\parallel}^2}$.

TR is always p-polarized which makes it a useful tool for polarizer calibration in our experimental setup. Using eq. 1.1 we can plot P_{TR} as function of wavelength (Fig. 1.4(a)).
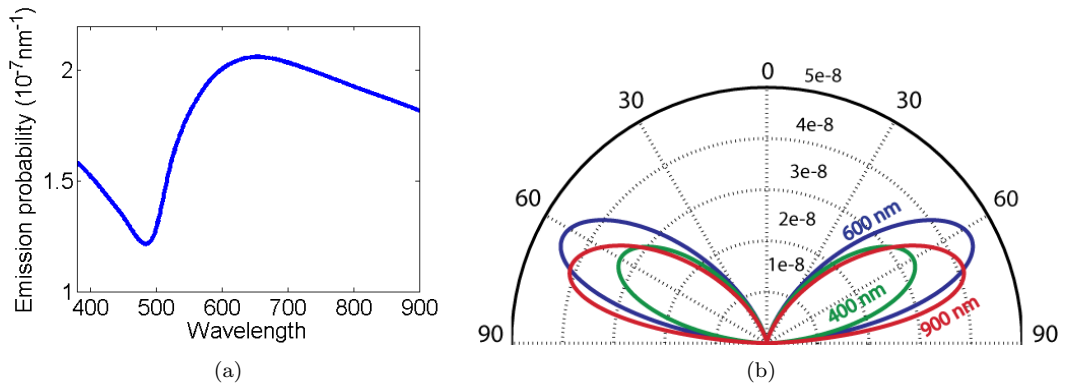
Figure 1.4: (a) TR-emission probability per incoming electron as function of wavelength. The probability is integrated over all angles. (b) Polarplot showing TR-emission for 400 nm (green) 600 nm (blue) and 900 nm (red). The radius represents the TR-emission probability per electron per degree

Tabulated values for ε_2 were used in this calculation [9]. We can see that the emission probability goes through a dip at around 490 nm. There is a peak at around 630 nm. The experimental TR-spectrum peaks at 600 nm which is consistent with the theoretical prediction.

Figure 1.4(b) shows $|\mathbf{f}(\theta)|^2$ for three different wavelengths. The TR radiation pattern resembles a toroidal radiation pattern of a point dipole except that it is bent upwards due to the gold substrate. The size of the lobes can directly be related to Fig. 1.4(a). Furthermore it can be seen that the radiation pattern becomes more grazing for larger wavelengths.

The generation of Cherenkov radiation, TR and SPPs is coherent with respect to the field of the incoming electron [4, 5]. The collective radiation produced by an electron beam through the coherent processes mentioned above, is called electron induced radiation emission (EIRE). In this thesis we will focus on metal structures and surfaces so for our experiments EIRE is the most important form of radiation but we will refer to it as CL because that is the convention in most of the scientific literature.

Chapter 2

Experimental setup

2.1 Introduction

The experimental setup described in this chapter collects cathodoluminescence from the vacuum chamber of a scanning electron microscope (SEM) that results from the impact of the electron beam onto a substrate. The microscope used is a FEI SFEG-XL30 scanning electron microscope (SEM) which is equipped with a Schottky field emission gun. The radiation produced by the electron beam is collected by a highly reflective diamond-turned aluminum parabolic mirror with a nearly hemispherical acceptance angle of 1.43π sr. A hole in the mirror with a diameter of approximately 1 mm allows the electron beam to pass.

A substantial part of this project consisted of improving and upgrading the CL-system. For CL it is of paramount importance that the parabolic mirror is in focus. The electron beam must hit the sample exactly in the focus of the parabolic mirror which is diffraction limited for a perfectly shaped paraboloid. For this purpose, an accurate alignment tool was implemented. The new setup also added angle-resolved detection of CL and extended possibilities to filter the CL-emission.
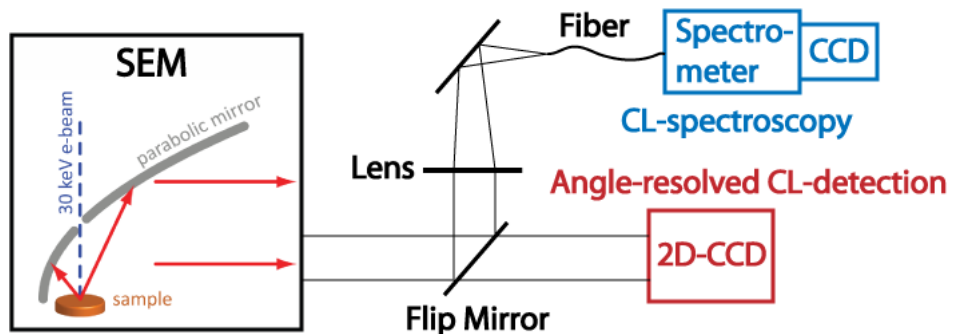
Figure 2.1: Schematic drawing of the experimental setup. The apparatus for spatially resolved CL-spectroscopy is shown in blue while the apparatus for the angular-resolved emission detection is shown in red.

2.2 Experimental setup

A schematic drawing of the new experimental setup is shown in Fig. 2.1. There are distinct optical pathways for the two different types of detection (indicated in red and blue in Fig. 2.1). Using a motorized flip mirror it is possible to switch automatically between these two pathways. In between the SEM and the flip mirror there is room for additional optics like polarizers and bandpass filters.

This is achieved by accurately positioning the mirror and the sample. To resolve this problem, an accurate mirror-positioning system was developed and built at AMOLF. It consists of four piezoelectric stepper motors with a dynamic range of ∼1 mm which push against and pull on a titanium leaf spring mechanism. A drawing of this arrangement is shown in Fig. 2.2(a). The spring system is mounted on an aluminum table which can be installed in the SEM-chamber in only one minute (Fig. 2.2(b)). The table rests on three points and is fixed by tightening one screw. The piezos are connected with their controllers with a connector attached to a vacuum feedthrough. At the moment it takes a few minutes to connect the piezos because it is difficult to get the connector into the steel pipe to which the feed through is attached because it is too narrow. The piezo controllers are connected to a PC from which they are controlled by a LabVIEW program. Figure 2.2(c) shows the SEM-chamber during an experiment with the mirror system installed. After finishing an experiment the piezos are disconnected and the table is removed (± 5 min), leaving an empty SEM-chamber for the next user.

The spring system allows positioning in four dimensions (x, y, pitch and yaw as indicated in Fig. 2.3) with high precision. The distance from the sample to the mirror can be adjusted with the SEM stage which already had ∼10 μm precision.

2.3 Direct imaging of the parabolic mirror

2.3.1 Focusing of the parabolic mirror

If the flip mirror is down, there is a direct path from the parabolic mirror to a back-thinned peltier-cooled pixis imaging charge coupled device (CCD) array with 1340 x 400 pixels allowing us to directly image the beam coming from the SEM chamber. If the mirror is in focus the beam emanating from the mirror is parallel because all the optical path lengths from

| (a) | (b) | (c) |
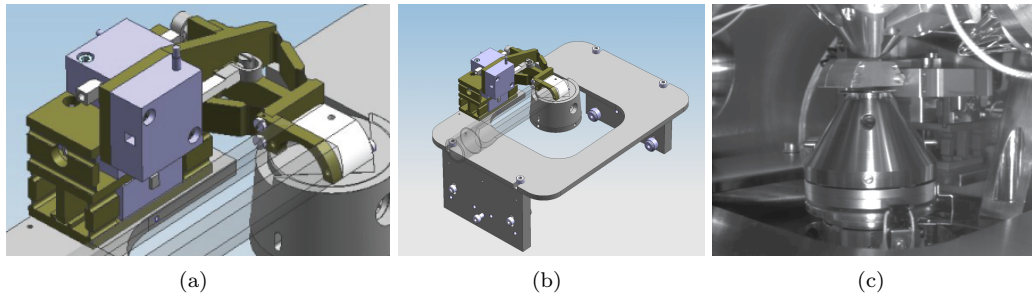
Figure 2.2: (a) The titanium leaf spring system with parabolic mirror. (b) The spring system on the aluminum table which can be mounted in the SEM-chamber. (c) Image of the Cl-table in the SEM-chamber during a measurement session.
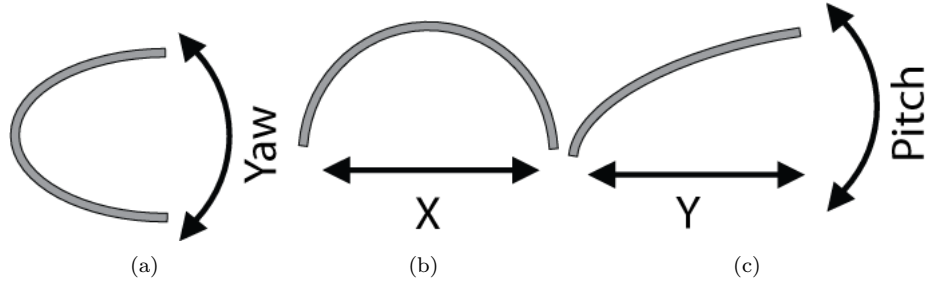
Figure 2.3: Micropositioning of the mirror in four dimensions. For clarity three different perspectives are shown which only show the mirror contours: (a) top view (b) front view (c)side view.

sample to detector are equal. Furthermore the shape of the beam exactly matches the front face of the mirror which has a nearly semicircular shape (Fig. 2.4(a)). If the mirror is not in focus, this shape is highly distorted (Fig. 2.4(b,c)), but we can recognize from the distorted image which way to move the mirror using raytracing results for various misalignments (Fig. 2.4(d-f)). The dark circle observed in the center of Figs. 2.4(a,c) is due to the hole in the mirror for the electron beam. The hole is approximately centered above the mirror focus.

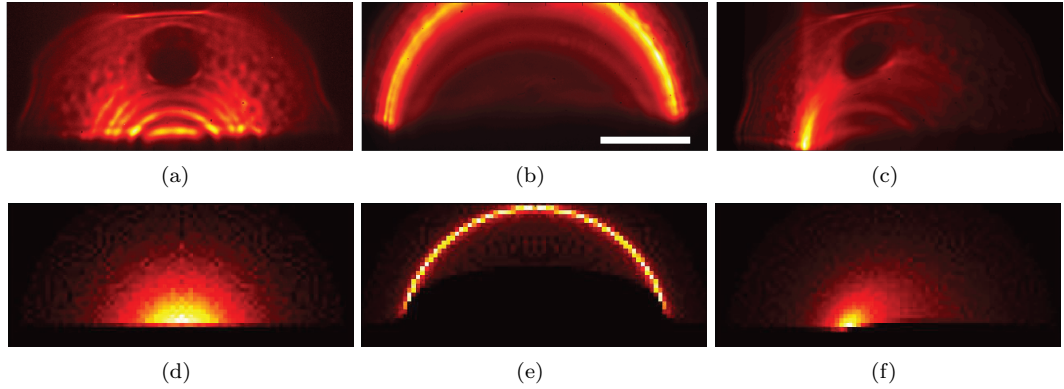**Figure 2.4:** CCD image when the mirror is (a) in focus (b) misaligned in y and (c) misaligned in x with corresponding raytracing results (d-f). The color indicates the CL-intensity and the scale bar is 5 mm.

To optimize the focus it is convenient to start with coarse displacements (typically 5 to 10 piezosteps where one step corresponds to about 5 μm) to quickly approach the optimal mirror orientation. For the final fine tuning it is necessary to use single steps for y, yaw and pitch and even substeps for x. It is particularly difficult to find the right combination of pitch, y and z. Ideally, the focus is at the eucentric point of rotation. However, due to a flaw in the design, the focus is slightly above the eucentric point and as a result pitch and y are not decoupled during alignment. Another problem is that when the system is aligned close to the optimal focus a misalignment in z looks very similar to a misalignment in y. By making small steps back and forth in both dimensions this problem is resolved and it is possible to obtain a good alignment but it takes a few minutes. We use this alignment procedure for both spectral and angle resolved Cl-measurements

2.3.2 Quality of the parabolic mirror

If we look more closely at Fig. 2.4 (a) we see that the detected wavefront has quite an irregular shape. There are dark concentric rings in the intensity which are centered around the optical axis of the mirror. These fringes are probably due to the diamond turning fabrication process which introduces concentric irregularities and a limited curve accuracy. The curve accuracy of this mirror is specified to be 2λ @633 nm which, according to the manufacturer, is consistent with the number of fringes in our CCD images. We also see smaller spot-like abberations which are probably caused by smaller imperfections in the mirror. Finally, we notice that the hole in the mirror for the electron beam appears to be very big in the CCD. By imaging the hole using the SEM we established that this is due to the fact that the area around the hole was damaged during the drilling of the hole. By moving the CCD closer to the mirror the hole appears to get smaller suggesting that the radiation coming from that part of mirror is not sent out entirely parallel. This confirms the hypothesis that the mirror surface is damaged/warped around the hole.

2.3.3 Resolving angular emission patterns

If the mirror is well-focused, each pixel in the CCD image corresponds to a single point (or very small area) on the paraboloid. Each point on the paraboloid is associated with a unique emission angle which can be described by a zenithal angle θ running from 0 to $\pi/2$ (where $\theta = 0$ is normal to the surface) and an azimuthal angle ϕ running from 0 to 2π (where the parabola vertex is at $\phi = \pi$). Therefore it is possible to extract the angular emission pattern of a source within the mirror focus from a CCD image. In order to do this it is necessary to calculate the angles associated with each point on the paraboloid.

By using the geometry of the mirror this can be achieved in a relatively simple way. Equation 2.1 shows how to convert from CCD pixels to coordinates on the paraboloid where the coordinates x_{pixel} and y_{pixel} describe a particular CCD pixel on the CCD array. x describes the position along the symmetry axis of the parabola, y describes the position in the lateral direction (Fig. 2.5(a)), z describes the height (Fig. 2.5(b)), r is the radial coordinate which can be calculated from y and z, d is pixel size (20 μm for this CCD camera) and a is the parabola coefficient (1/10 for our mirror).

(a)   (b)
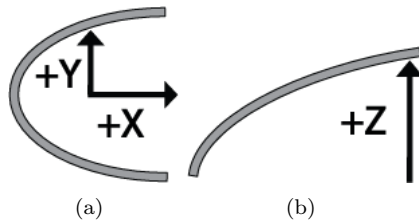
Figure 2.5: Coordinates used to describe parabola geometry.

(a)   (b)   (c)

(d)
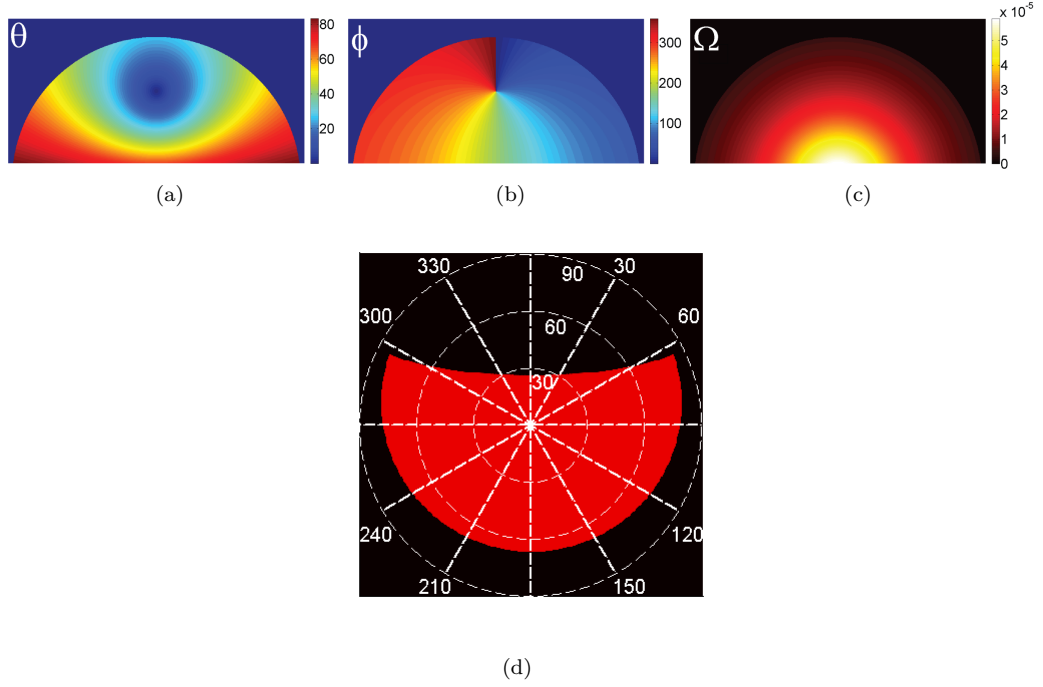
Figure 2.6: Maps allowing conversion from CCD pixels to (a) θ and (b) ϕ (c) with a correction for the solid angle. (d) Polarplot for an isotropical emitter using the conversion maps shown above.

$$y = x_{pixel} \times d \tag{2.1a}$$

$$z = y_{pixel} \times d \tag{2.1b}$$

$$r = \sqrt{y^2 + z^2} \tag{2.1c}$$

$$x = ar^2 - \frac{1}{4a} \tag{2.1d}$$

Using trigonometric relations, θ and ϕ can be calculated for every CCD-pixel.

$$\theta = \cos^{-1}\left(\frac{z}{\sqrt{x^2 + r^2}}\right) \tag{2.2a}$$

$$\phi = \tan^{-1}\left(\frac{y}{x}\right) \tag{2.2b}$$

Figures 2.6(a,b) show a map of the CCD pixels onto θ and ϕ. The amount of solid angle per CCD pixel is not constant due to the curvature of the mirror. Figure 2.6(c) shows the solid angle covered per pixel.

$$\Omega(x_{pixel}, y_{pixel}) = d^2(x^2 + r^2)\frac{2ar^2 - x}{(x^2 + r^2)^{\frac{3}{2}}} \tag{2.3}$$

Summing over the relevant pixels gives a total acceptance angle of 1.43π sr. Using the pixel-to-angle mapping, the solid angle correction and linear interpolation, the intensity as function of angle can be represented in a polar plot, as shown in Fig. 2.6(d).

2.4 Spatially resolved cathodoluminescence spectroscopy

2.4.1 Spectral imaging of cathodoluminescence

A Gatan Digiscan II controller unit is used in conjunction with the software package Digital Micrograph to scan the electron beam over the desired area on the sample. It is possible to scan points, lines or areas. Light that is emitted from the sample is collected by the parabolic mirror. During spatially resolved spectroscopy the flip mirror is up directing the light to a lens with a focal distance of 100 mm, which focuses the light onto a 600 μm core diameter optical fiber. The fiber guides the light to a PI ACTON SP2300i spectrometer where the light falls onto a grating which decomposes the CL into different colors through diffraction, after which it is spectrally resolved with a liquid nitrogen cooled front-illuminated EEV 100x1340F charge coupled device camera from Roper scientific. Normally hardware binning is performed 100 times vertically and 4 times horizontally to increase the measurement speed and SNR, effectively leaving an array of 1 x 335 pixels.
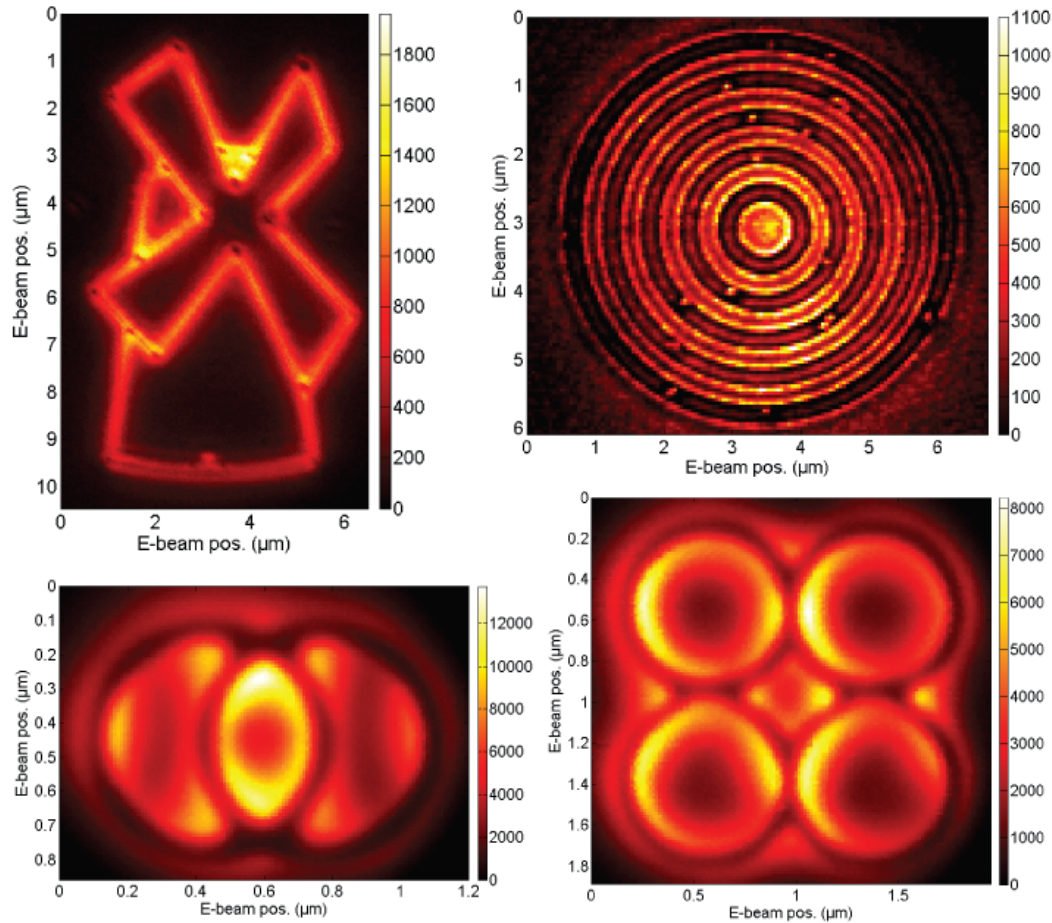
Figure 2.7: examples of scans with large numbers of scanning pixels, performed on structures fabricated in gold and silver using focused ion beam miling. A mill, a bullseye grating, a set of overlapping v-groove ring resonators and quartet of v-groove ring resonators are shown respectively.

Because the alignment of the mirror can be perfectly monitored and controlled we can collect ∼15x more CL-signal than in the old system. This allows much faster scanning (down to 0.01 s/pixel) making it possible to routinely do high quality 2D scans with a large number of pixels in a short amount of time. Figure 2.7 shows four examples of such scans, illustrating that CL can be used as high resolution imaging tool, imaging structure on a surface, including small defects which can for instance be seen in the bullseye grating (top-left scan). These kind of images are typically acquired within 15 minutes with 0.05 seconds integration time per pixel.

2.4.2   Electron beam settings

The acceleration voltage of the electron beam can be varied from 0.5 kV to 30 kV and the beam current can be tuned as well. In general the acceleration voltage was set to 30 kV to optimize the spatial resolution and the amount of CL signal [5]. The beam current can be varied by changing the spot setting or the aperture. Table. 2.1 shows beam current for different settings. The currents were measured using a faraday cup.

**Table 2.1:** Beam current for different beam settings

Aperture	Spot	Current (nA)
3	6	13.2
3	5	10.8
3	4	4.39
6	6	1.25
6	5	0.973
6	4	0.390

The optimal beam current can vary per experiment. Although working with lower beam currents yields a superior spatial resolution, higher currents give a better signal- to-noise ratio (SNR) for the same acquisition time per pixel. For the experiments which require <20 nm resolution the aperture has to be set to 6. When using the highest beam current the resolution is closer to 30 nm blurring sharp features like edges.

For angular resolved measurements it usually necessary to use the highest beam current to obtain a reasonable SNR, especially when a color filter or polarizer is used.

2.4.3   Polarization sensitive detection

During polarization sensitive detection there is a polarizer in the beam path. Using a slit, the centerline of the mirror along the optical axis is selected where the emission polarization is not significantly altered. In Fig. 2.8(a) the black box indicates the position of the slit. By rotating the polarizer the p-polarized TR-emission from a metal surface can be minimized or maximized. By minimizing the TR-emission we select horizontally polarized light emission while by maximizing the TR-emission we select vertically polarized light emission. Figure 2.8(b) shows how vertical and horizontal polarization are defined with respect to the parabolic mirror. Note that the slit blocks a substantial part of mirror which in combination with the polarizer results in much lower CL-signal levels. Additionally, when you have an emitter with a dipole moment in the plane of the substrate and parallel to the slit, the toroidally shaped emission is not collected effectively because the slit blocks most of these
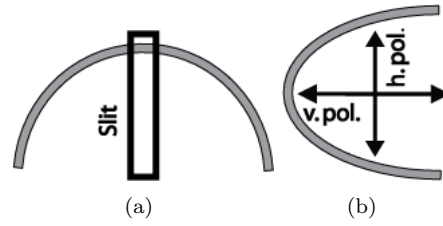
Figure 2.8: (a) Front view of the parabolic mirror indicating which part of the mirror is selected by the slit. (b) Top view of the mirror showing how vertical and horizontal polarization are defined.

emission angles. This can be solved by rotating the stage with 90° degrees.

2.4.4 Detection efficiency
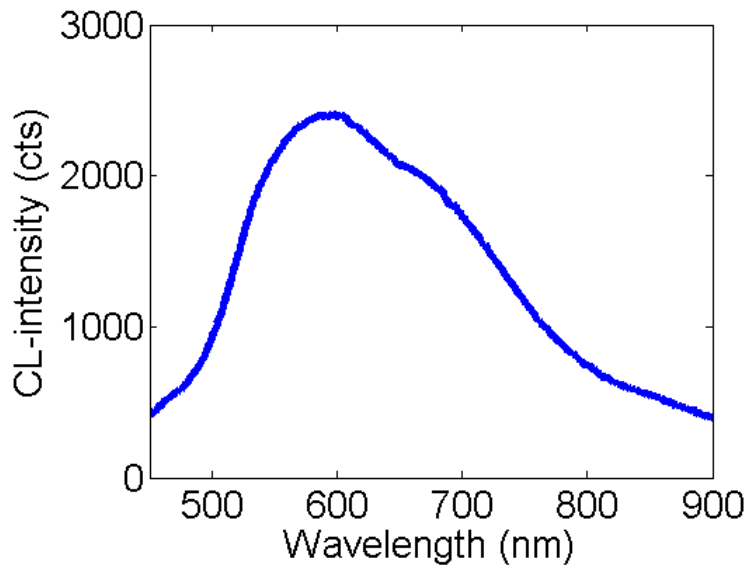
Figure 2.9: TR spectrum from a single crystal gold substrate measured with a beam current of 13.2 nA. The integration time was 1 second.

The theory for transition radiation is well-understood. Using the equations from chapter 1 we can calculate that on gold $7.65 \cdot 10^{-5}$ TR-photons are emitted per incoming 30 keV electron for a wavelength range of 500-900 nm. This was calculated using tabulated values for ε [9].

We can estimate the losses in the different components of the setup. The parabolic mirror only collects 1.43π sr (71% of the hemisphere) and is not a perfect reflector ($\sim$80% collection efficiency). The radiation pattern of the TR is not taken into account in this estimate. Using the response curves of the grating supplied by the manufacturer, the average efficiency of the spectrometer is estimated to be $\sim$60% and the average quantum efficiency for the CCD camera is estimated to be $\sim$30%. The loss in the optics is approximately 3% per glass-air

interface resulting in a total efficiency of $\sim$84% Combining these efficiencies we find that the system should have a detection efficiency of $\sim$8.6%.

Using the new system, a TR-spectrum on single-crystalline gold was collected with an integration time of 1 second at a beam current of 13.2 nA, which corresponds to $8.25{\cdot}10^{10}$ e$^-$. The spectrum is shown in Fig. 2.9.

To obtain the detection efficiency first we integrate our experimental TR-spectrum over wavelength from 500 to 900 nm. Depending on the gain settings of the CCD, a certain number of electrons is necessary to produce a single count on the CCD. In this case the gain is set to the highest value which corresponds to 1e$^-$/count. Multiplying by this number gives the total amount of photons detected by our setup. We find that the total number of collected photons is $3.5{\cdot}10^5$. Subsequently we divide this by the number of photons predicted by theory, which is the number of electrons $(8.25{\cdot}10^{10})$ times the photon excitation probability per electron $(7.65{\cdot}10^{-5})$. We find that the detection efficiency of our experimental setup is approximately 5.5%.

We can conclude that the system efficiency is already quite close to what we expect for this equipment, which is a promising result. Especially when we consider that in the old system the collection efficiency was 15 times lower corresponding to a detection efficiency of $\sim$0.35%).

2.5 Outlook

Although a lot of progress has already been made with this new setup there is still plenty of room for improvement. A second upgrade, where several parts will be replaced is scheduled to be performed in the near-future.

In this upgrade the current parabolic mirror will be replaced by a custom made mirror with a larger acceptance angle, a smaller hole of only 600 μm and a higher curve accuracy ($\lambda/2$ @633nm). It is expected that this will improve the quality of angle-resolved measurements and increase the total amount of light collected during CL-spectroscopy measurements.

Additionally, the optics box will be replaced by a sturdier version, reducing the amount of vibrations which are detrimental to high-resolution SEM-imaging and CL-measurements. It will also be much easier to hermetically seal this box, thereby excluding all ambient light from the experiments. The piezomotor vacuum feedthrough will be replaced as well to make the cable connections more robust.

The air cooled Pixis camera will be replaced by a water cooled Pixis camera which also reduces vibration levels and prevents potentially harmful heat buildup in the enclosed optics box. This camera will be synchronized with the SEM-pixelscanning, simplifying spatially resolved angular emission pattern measurements.

Chapter 3

Influence of FIB milling on the propagation length of SPPs

3.1   Introduction

Surface plasmon polaritons (SPPs) are electromagnetic waves confined to a metal-dielectric interface [10]. SPPs can be manipulated by making waveguide and resonator structures on metals. Focused-ion-beam (FIB) milling is a technique that is used commonly in plasmonics to make these structures on metals. Unlike e-beam lithography, nanoimprint lithography, self assembly or templating techniques FIB milling is essentially a one-step process [11].

In a typical FIB device Ga^+ ions from a liquid ion source are accelerated to 30 keV and focused onto a sample by an electrostatic lens. The impinging ions sputter material from the surface of the sample. Because the spot-size diameter can be as small as 5 - 10 nm, FIB milling is an accurate process. Combined with its simplicity this makes it an ideal technique for the maskless fabrication of nanoscale plasmonic components [11]. The milling-rate depends on the crystal orientation, so for the fabrication of smooth structures it is preferable to use samples which are single-crystalline. In this experiment a single-crystal gold sample of 1 mm thickness was used which is effectively semi-infinite for optical fields.

During FIB milling part of the high-energy Ga^+ ions is trapped in the top layer of the sample. At the same time material is sputtered from the surface of the sample. The concentration of gallium ions in the top layer of the sample increases until an equilibrium is reached between the trapping and sputtering of ions. The absorption of gallium ions could possibly alter the optical properties of the surface. This could have consequences for the propagation of SPPs on the surface of the sample. Additionally, FIB milling can cause an increase in surface roughness which has a negative influence on SPP propagation [10]. In this experiment we investigate whether FIB milling has a significant influence on SPPs. We compare the SPP propagation length on an untreated gold surface with the propagation length on gold surfaces that have been subjected to FIB milling.

3.2   Experiment

Seven rectangles of 100 x 75 μm were milled into the gold with depths of respectively 0.1 nm, 0.13 nm, 0.26 nm, 1.03 nm, 5.13 nm, 10 nm and 500 nm relative to the surface. Then gratings were milled into these rectangular surfaces and one extra grating was milled in the
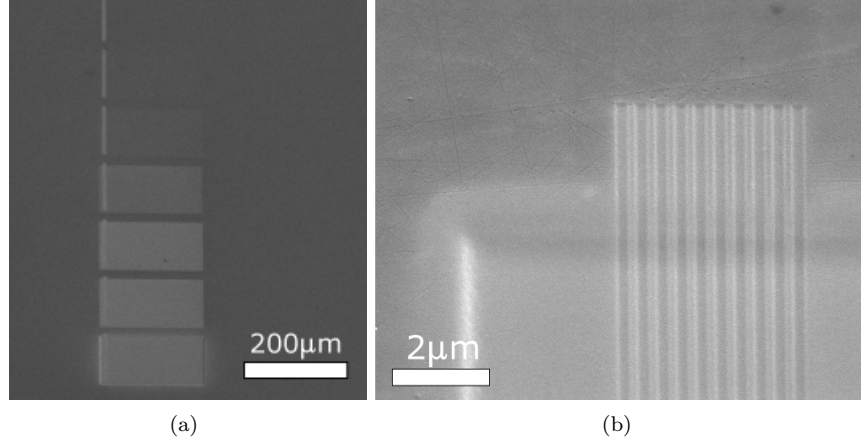
Figure 3.1: (a) Overview SEM micrograph of the seven milled surfaces with depths of 0.1, 0.13, 0.26, 1.03, 5.13, 10 and 500 nm. The depth of the rectangles increases from top to bottom. (b) SEM micrograph of the upper left corner of the deepest rectangular surface. The grating can clearly be distinguished.

untreated gold (depth 0) as a reference. The gratings consist of ten 50 nm deep, 200 μm long and 250 nm wide square grooves with a pitch of 500 nm. A SEM micrograph of all the surfaces and gratings is shown in Fig. 3.1(a). The gratings are located at the left side of each milled region.

Figure 3.1(b) shows a SEM micrograph of the deepest milled region, with grating, at higher magnification. It can clearly be seen that the surface still appears very smooth after milling. This is important because an increased roughness due to the milling process influences SPP propagation.

We used cathodoluminescence (CL) imaging spectroscopy to measure the SPP decay length. These measurements were performed using a FEI XL-30 scanning electron microscope (SEM) equipped with a Gatan paraCL cathodoluminescence system. The 30 kV electron beam of the SEM acts as an SPP source. In addition to SPPs the beam also generates transition radiation (TR) [12].

The gratings couple out the SPPs produced by the electron beam as far field photons. This light is collected by a parabolic mirror and then sent through a monochromator after which it is spectrally resolved with a liquid-nitrogen cooled charge coupled device (CCD) array.

The CL-intensity was measured as function of distance from the grating by scanning the electron beam along a line perpendicular to the grating normal. This was done for all eight gratings. The electron beam was scanned away from the grating (from left to right in Fig. 3.1 (a)). At each pixel of the line scan an entire (visible) spectrum was measured yielding a 3D-dataset (wavelength, distance, intensity). The measurements were corrected for the TR-background, system response and the dark counts in the CCD afterwards.

As the electron beam moves further away from the grating, the SPPs have to propagate further to reach the grating. Due to Ohmic losses in the metal and scattering caused by small imperfections in the gold, the number of SPPs that reach the grating diminishes as
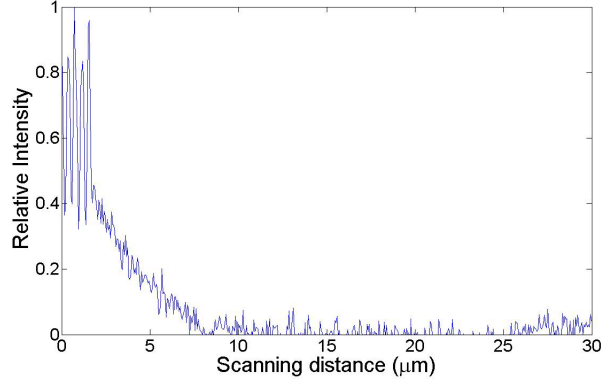
Figure 3.2: Cl intensity as function of distance for the untreated surface, measured at a wavelength of 600 nm with 10 nm bandwidth.

the beam moves away from the grating. As a result the number of photons that are coupled out decreases resulting in a drop in CL-intensity [13]. The size of the rectangle ensures that plasmon reflections from the boundaries are not important for the measured intensity. In Fig. 3.2 a line scan is shown of the first grating (untreated surface). In this plot we have taken 600 nm as the center wavelength and we have integrated over a bandwidth of 10 nm to reduce the noise. This particular center wavelength was chosen because the CL-intensity was highest here yielding the best signal-to-noise ratio. The oscillations in the first two microns are due to the grating. The CL intensity clearly decays with distance.

The electron beam is a point source of SPPs and consequently the SPPs can propagate towards the grating over a large range of angles. We have already subtracted the TR from the data and normalized it in which case the CL intensity as function of distance is given by

$$I(x) = \alpha(\theta) \int_{-\pi/2}^{\pi/2} e^{-x/(L_{SPP} \cos(\theta))} \, d\theta \qquad (3.1)$$
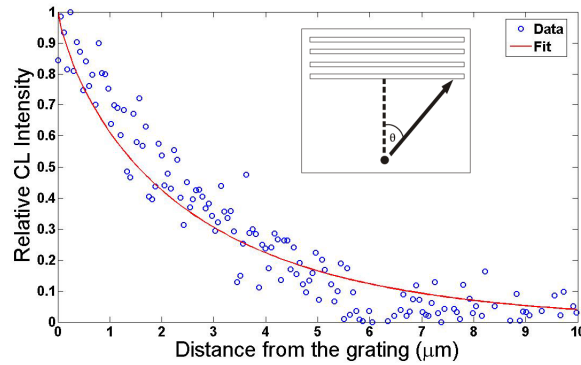
Figure 3.3: Equation 1 fitted to the normalized CL data measured for $\lambda = 600$ nm and a bandwidth of 10 nm. The inset schematically shows a SPP, originating from a point source, propagating towards the grating at an angle θ from the normal.

where x is the distance from the grating, θ is the angle between the SPP propagation direc-
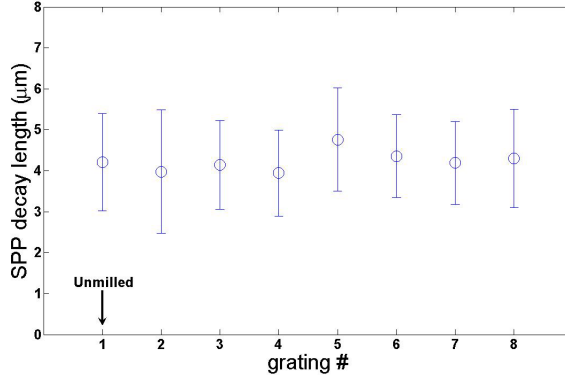
Figure 3.4: Decay lengths for the different surfaces. The arrow indicates the untreated surface. Grating 2 represents the shallowest rectangular surface (treated with the lowest ion dose) while grating 8 represents the deepest rectangular surface (treated with highest ion dose).

tion and the grating normal (see inset in figure 3.3), L_{SPP} is the 1/e decay length and $\alpha(\theta)$ is the angle dependent grating coupling efficiency [14]. In this case we assume that $\alpha(\theta) = 1/\pi$ so the coupling to the grating is angle-independent in this case. To obtain the 1/e decay length for all eight surfaces, equation 1 was fitted to the CL-data at the region excluding the grating area. Figure 3 shows such a fit for the first grating. This fit corresponds to a decay length of about 4 μm.

For wavelengths smaller than 550 nm and larger than 630 it was not possible to do a good data fit because the signal-to-noise ratio was too small in these regions. In Fig. 3.4 the decay lengths, obtained from fitting equation 1 to the data, are plotted for the different gratings.

3.3   Conclusion

There appears to be no correlation between the milling depth and SPP-decay length. Also the difference between the untreated and milled surfaces is small. This suggests that the remaining surface roughness after FIB milling and the gallium ions trapped in the gold do not noticeably hinder SPP propagation at 600 nm in single-crystalline gold. We expect that the SPP propagation at other wavelengths in the visible part of the spectrum is not significantly affected by FIB milling either.

It is important to mention that ohmic losses are very high for these wavelengths and it could be that the influence of the milling process on the SPP propagation length is within the measurement error. For infrared wavelengths the ohmic damping is not as strong and as a consequence the the SPP propagation lengths are much longer($\sim$190 μm for 1500 nm on gold). Because of the reduction in ohmic damping, it could be that the relative contribution to the total amount of loss in the material due to FIB milling is much larger. Therefore it could be that FIB milling has a significant influence on the SPP propagation length for higher wavelengths.

Nevertheless we can conclude from these experimental results that for visible frequencies, FIB milling is a non-distorting production method which is well suited for the fabrication

of plasmonic nanostructures with high optical quality.

Chapter 4

# Plasmon resonances in annular and elliptical groove resonators

4.1 From circular to elliptical plasmon resonators

4.1.1 Introduction

Surface plasmon polaritons (SPPs) are electromagnetic waves confined to a metal-dielectric interface. SPPs can be manipulated by resonant structures nanofabricated in metals. It has been shown that annular groove nanoresonators in gold can support surface plasmon whispering gallery modes originating from circulating metal-insulator-metal (MIM) groove plasmons which are strongly coupled across the metal plateau [15]. The spatial distribution and spectral shape of the plasmon modes is highly dependent on the radius, groove depth and groove width of the ring-resonator. Because light is tightly confined in the narrow grooves, these resonators have a high Q/V (ratio between quality factor and mode volume) which is of interest for the control of spontaneous emission and low-threshold lasing. In this experiment we investigate the evolution of plasmon modes when we gradually change the circular groove resonator into an increasingly more elliptical resonator.

4.1.2 Experiment

Using focused ion beam milling (FIB) a series in which a circular resonator changes into an increasingly elliptical resonator was milled into a Czochralski grown single-crystal Au substrate. We will label the resonators with integers 1 to 6 where resonator 1 is circular and resonator 6 is the most elliptical. The circular resonator have a radius of 200 nm (from the
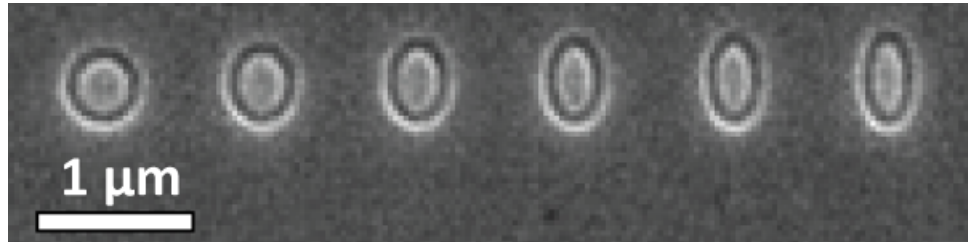
Figure 4.1: SEM micrograph of the resonators. The ellipticity increases from left to right.
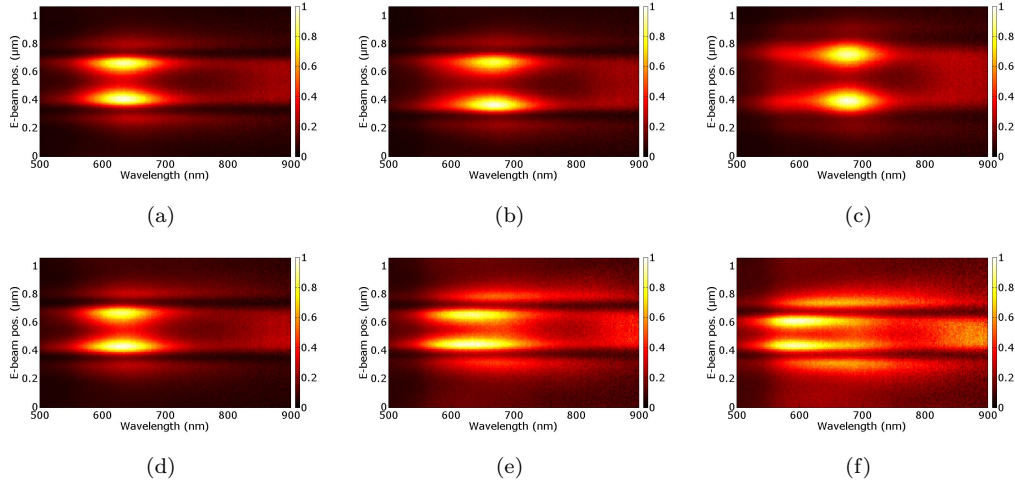
Figure 4.2: Line scans along the minor and major axis for (a,d) resonator 1, (b,e) resonator 3 (c,f) and resonator 6.

center of the resonator to the center of the groove), a groove width of 100 nm and nominal depth of 100 nm. The length major axis was increased in steps of 20 nm and the length of the minor axis was adjusted accordingly to maintain a constant circumference. A SEM micrograph of the resonators is shown in Fig. 4.1.

CL-emission from the resonators was measured as function of electron beam position by scanning the e-beam over the major and minor axis of the resonator along a line. Note that for a circular resonator, the major and minor axis have the same lengths. An entire spectrum was measured at each pixel. The measurements were corrected for the spectral response. Figure 4.2 shows line scans along the two orthogonal axes for resonators 1,3 and 6.

We can see that the spectral shapes of the resonances excited on the major and minor axis look very similar for resonator 1 which is to be expected due to its azimuthal symmetry. For the elliptical resonator however, the resonances along the two axes differ pronouncedly. The resonances excited on the minor axis become broader while the resonances excited on the major axis are redshifted and become narrower. To clarify the spectral change of the resonances for different ellipticities, the line scan spectra were summed and subsequently normalized (Fig. 4.3).

As expected the spectra measured along the major and minor axis are nearly identical for resonator 1. When the resonators become elliptical the spectra for major and minor axis are no longer equal. By changing the aspect ratio of the resonator the symmetry in the system is broken resulting in different spectra for the different axes.

Even though the linescans in Fig 4.2 already contain information about the spatial distribution of the field, a 2D spectral image is more intuitive and yields a more complete picture of the field distribution. Fig. 4.4 shows 2D spectral images of resonators 1,3 and 6 for λ=725 nm integrated over a 10 nm bandwidth.

In both spectral images there are equidistant dark vertical lines visible. This is caused by the spatial drift correction which was performed every five pixels. During the drift correction the
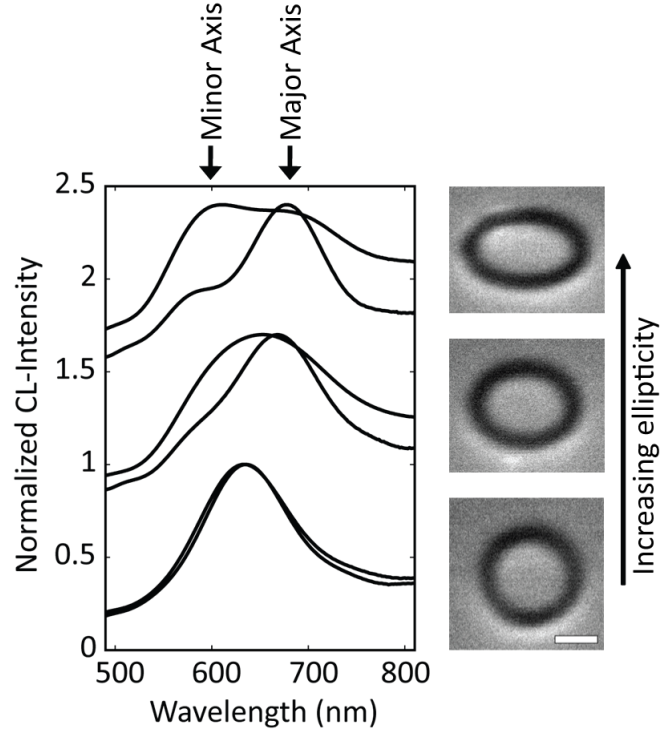
Figure 4.3: Normalized CL-spectra for major and minor axis for three different resonators. For clarity the peaks have been vertically offset. SEM micrographs of the corresponding resonators (1,3,6) are shown on the right of the figure (scale bar is 200 nm).

shutter in front of the CCD is closed, after which it reopens and the scan continues. While the shutter is still reopening the CCD already starts collecting light for the next scanning pixel, thereby slightly reducing the amount of collected light for that pixel. Additionally, the top-left quadrants of the scans seem to be relatively intense compared to the other quadrants which is attributed to a different collection efficiency for different polarizations of light.

As expected the 2D-excitation map for resonator 1 is approximately rotationally symmetric. In the maps for resonators 3 and 6 we see two intense lobes appear on the left and right side of the plateau so in these resonators the symmetry is broken. This lobe pattern is very
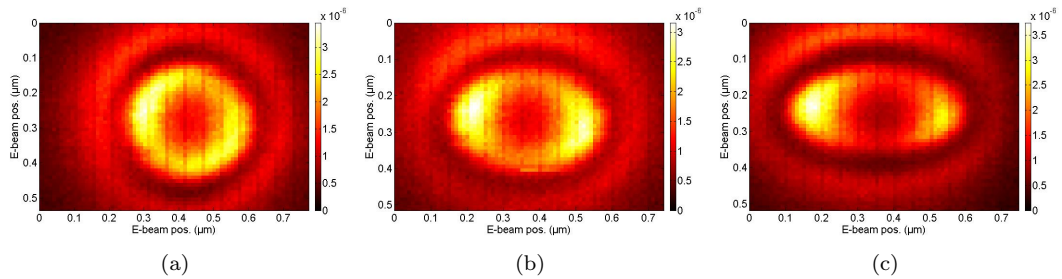
Figure 4.4: 2D Spectral image of resonator 1 (a), resonator 3 (b) and resonator 6 (c) for λ=725 nm integrated over a 10 nm bandwidth.

similar to the m=1, n=1 mode profile for circular resonators [15]. In a ring resonator these lobes cannot be seen due to the azimuthal symmetry of the system, unless a polarizer is used to select one particular polarization. In the elliptical resonator however, the symmetry is broken, making the dipolar mode profile discernible in the spectral image. Since this resonator has a relatively small major and minor axis we do not expect the quadrupolar m=2 mode to be pronounced in this system. For a larger resonator this mode becomes more important and it will be possible to see four lobes appear.

4.1.3 Conclusion

In conclusion, we have seen that by changing the resonator geometry from a ring to an ellipse, the spectral shape as well as the spatial distribution of the plasmon modes is altered. The change in geometry breaks the symmetry in the system, thereby lifting the degeneracy of plasmon modes excited along the major and minor axis of the resonator.

In this chapter it has become clear that besides resonator diameter, groove depth and groove width the spectral shape and spatial distribution of plasmon modes also depends strongly on the ellipticity of the resonator. This gives us yet another degree of freedom to precisely engineer the mode structure of these nanoresonators, which could prove to be useful for future applications.

4.2   Coupling of annular groove plasmon resonators

4.2.1   Introduction

Plasmon resonances in individual annular groove resonators in single crystal gold are well understood [15]. From boundary element method (BEM) calculations it is known that most of the fields are confined strongly to the bottom of the grooves.

In this experiment we investigate the coupling between two annular groove resonators. We vary the ring-separation and check if this alters the spatial distribution of the fields and/or the CL-emission spectra. For small separations the grooves overlap, potentially allowing the plasmons from the individual resonators to interact.

4.2.2   Experiment

Two series of double ring resonators with varying separation were fabricated in a single-crystalline Au surface using FIB milling. Also, single rings were milled as a reference. The resonators for both series have a groove width of 100 nm and a nominal depth of 100 nm but they have different radii of 150 and 300 nm where the radius is defined as the distance from the center of the disc to the center of the groove. The ring separation which is defined as the smallest separation between the two metal plateaus, was varied in steps of 5 nm. At around 100 nm separation the section of the groove that should isolates the plateaus starts to fill up with metal. This merges the metal discs at which point they are no longer individual groove resonators. Figure 4.5 shows SEM micrographs for two sets of rings with radii of 150 and 300 nm respectively. The ring separation is 110 nm for both sets.

CL-emission from the reference rings and the double rings was measured as function of e-beam position by scanning the e-beam over the resonators along a line in 10 nm steps. An entire spectrum was measured at each pixel. The measurements were corrected for the system response. In Figs. 4.6(c-h) the emission probability as function of e-beam position and wavelength is shown for separations of 200, 150 and 110 nm. For comparison, the reference scans are also included (Figs. 4.6(a,b)). The ring separation does not seem to have a strong influence on the field distribution in the resonator. We do not observe a significant difference between different separations. There is also no clear difference between the double rings and the reference rings.


(a)   (b)
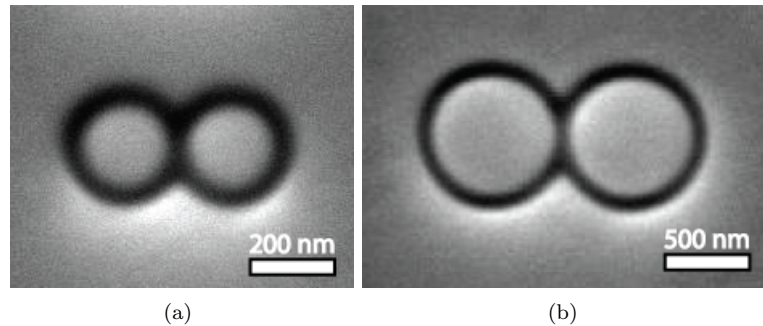
Figure 4.5: (SEM micrographs of two sets of double rings with a separation of 110 nm (a) for R = 150 nm (b) for R = 300.
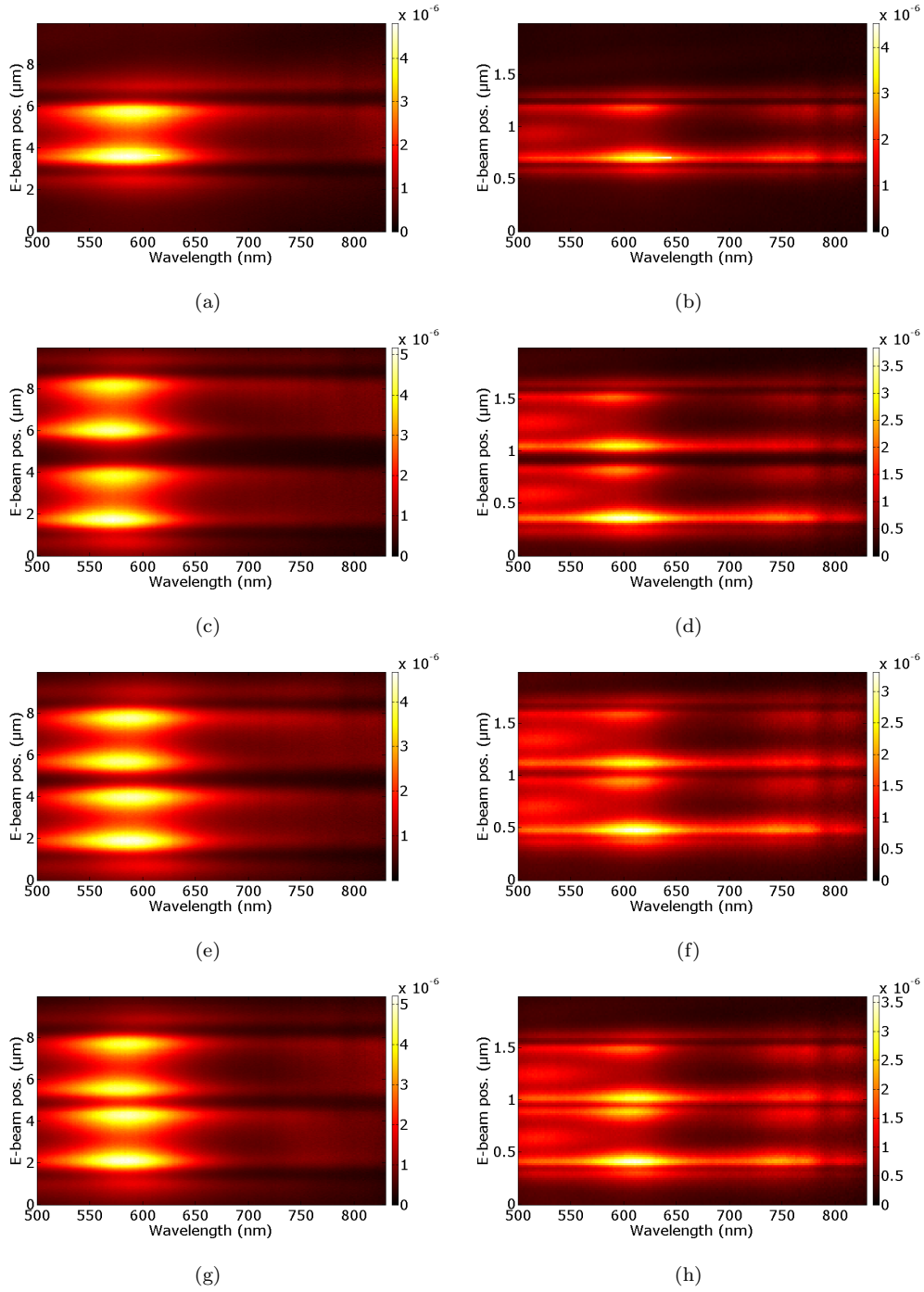
Figure 4.6: Line scans measured with 10 nm resolution showing emission probability as function of e-beam position and wavelength for a single ring and double rings separated by 200,150 and 110 nm (a,c,e,g) with R = 150 nm (b,d,f,h) with R = 300 nm.

To study the spectral behavior more closely the line scan spectra were summed and divided by the number of scanning pixels yielding the average emission probability as function
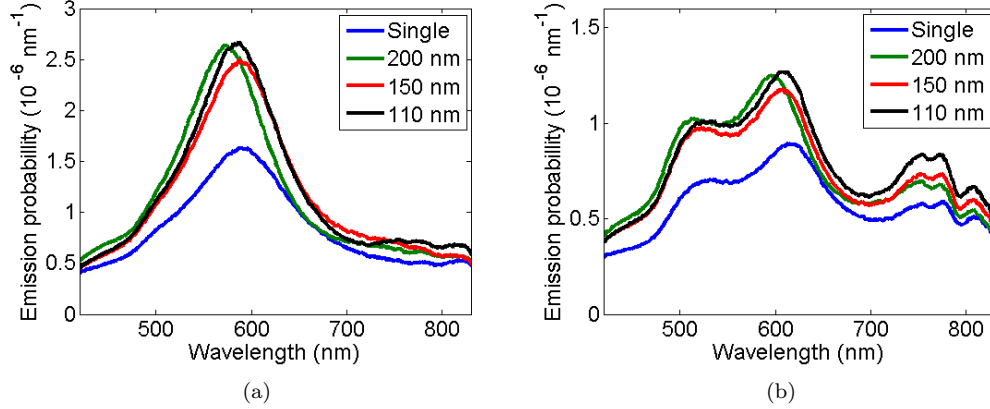
Figure 4.7: CL-spectra showing emission probability as function of wavelength for a single ring and double rings with a separation 200,150 and 110 nm (a) with R = 150 nm (b) with R = 300 nm. The legend indicates the ring separation.

of wavelength. The resulting CL-spectra are shown in Fig. 4.7.

The total intensity of the single reference rings is of course lower than for the double rings but the overall spectral shape is very similar. There are some minute variations but the separation does not significantly influence the CL-emission from the resonators. Even for the smallest separation where the grooves overlap almost completely, the spectral shape of the CL-emission is still nearly identical to the single reference ring.

4.2.3 Conclusion

We can conclude that for these particular resonators, inter-resonator coupling does not have a strong effect on the CL-emission. The results show that the field in the ring resonators is very well confined to the groove, making the resonator very stable and insensitive to its dielectric environment.

Possibly the effect of the coupling is within the error margins of fabrication and measurements. It could be that the radii, groove widths and groove depths chosen in this experiment are not optimal for strong coupling but the fact that we do not observe any effect makes it unlikely that other geometries will show strong coupling effects.

Chapter 5

Angular emission pattern of a single crystal gold ridge

5.1   Introduction

The influence of metal nanorod antennas on the directionality and lifetime of fluorescence has been extensively studied both with far-field and near-field light excitation [16–18]. The light excitation spot (even for NSOM) is too large to study the influence of an antenna on a single emitter close to the structure. Additionally, the spatial resolution of these techniques is insufficient to clearly resolve the mode structure on the nanorods since the field-strength variations occur on very short length scales (<50 nm).

In this experiment we study a single-crystalline gold ridge of 100x600 nm, fabricated with focused-ion-beam (FIB) milling. Figure. 5.1 shows a SEM micrograph of the structure. Such a ridge shows strong similarities with metal nanorods and its mode structure has been well studied with CL-spectroscopy [11] in the past.
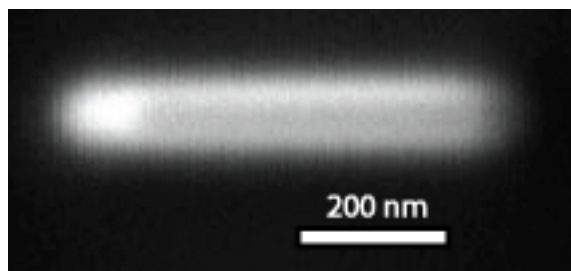
Figure 5.1: SEM micrograph of the ridge milled in single crystalline Au with FIB.

Here we will measure the angle-resolved CL-emission from a nanoantenna for the first time. The electron beam in our SEM has a spot size of only 10 nm allowing us to resolve mode structure with very high spatial resolution. We will use the point-like excitation of the electron beam to resolve the radiation pattern as function of excitation position with ∼10 nm spatial resolution. This will possibly give us more understanding of how single emitters like molecules interact with such a metal antenna perhaps allowing us to exactly tailor the emission of single emitters which in the future might lead to many applications.

Structures fabricated in single crystalline gold are convenient for CL-experiments because they exhibit excellent optical properties, generate strong CL-emission and TR-background upon electron beam irradiation. Additionally the ridge is fixed to the gold substrate which works as an effective heat sink, allowing the use of high beam currents without inflicting damage to the structure.

Analogous to freestanding nanorod antennas, the ridge acts as a Fabry-Pérot resonator for surface plasmon polaritons (SPPs) which are confined to the top of the ridge. The two end facets act as mirrors. This creates standing waves for particular plasmon wavelengths. The plasmon excitation probability is strongly connected to the field strength of local resonances. The standing plasmon waves on the ridge are characterized by a linear arrangement of nodes and antinodes making it possible to clearly resolve the Fabry-Pérot modes with CL-spectroscopy [11, 19, 20].

5.2 Experiment

### 5.2.1 Mode structure of the plasmon resonator

For analysis of the mode structure, a spectral image of the structure was performed with 10 nm resolution. At particular wavelengths a clear modulation of the CL-intensity can be distinguished along the ridge. These correspond to Fabry-Pérot modes where an integer number of half plasmon wavelengths fits into the resonator. Figure 5.2 shows cross sections of the spectral image with a 10 nm bandwidth for 600 nm, 750 nm and 910 nm.

At 910 nm there are 2 peaks can clearly be distinguished which might correspond to a $\lambda_{spp}/2$ resonance (m=1), while at 750 nm there are three peaks corresponding to a λ_{spp} (m=2) resonance. At 600 nm four peaks can be discerned corresponding to a $3\lambda_{spp}/2$ resonance (m=3). The mode profile can be clarified by making line cuts through Figs. 5.2(a-c) along the main ridge axis, yielding line profiles of the three modes (Fig. 5.3). Upon reflection the SPPs pick up a phase shift and this has an influence on the peak spacing. The phase pickup can vary as function of wavelength and cannot be predicted in a simple manner. Only the length of first period from the ends is influenced so for modes with m≥3 there are one or more periods which have a $\lambda_{spp}/2$ spacing [20].

The effect of the phase pickup is clearly visible in the standing wave pattern at 600 nm (m=3 resonance). In this case the spacing between the outer peaks is roughly two times smaller than the spacing between the central peaks. The spacing between the two central peaks is not influenced by the phase pickup and should correspond. By dividing the free space wavelength by the plasmon wavelength we find a mode index of 1.3. For the $m=1$ and $m=2$ modes at 910 nm and 750 nm it impossible to extract a reliable λ_{spp} because there are no periods in the standing wave pattern that are unaffected by the phase pickup. Equation. 5.1 [21] describes at what width a Fabry-Pérot resonance is expected

$$W_{res} = \frac{m - \phi(\lambda_0)/\pi}{2} \cdot \frac{\lambda_0}{n'_{spp}} \qquad (5.1)$$

where λ_0 is the free space wavelength, m is the mode order, $\phi(\lambda_0)$ is the phase pickup, n'_{spp} is the mode index and W_{res} is the resonance width which is equal to the length of the ridge. We can find the phase pickup at 600 nm by rewriting eq. 5.1 yielding a phase pickup of $2\pi/5$

(a)

(b)

(c)
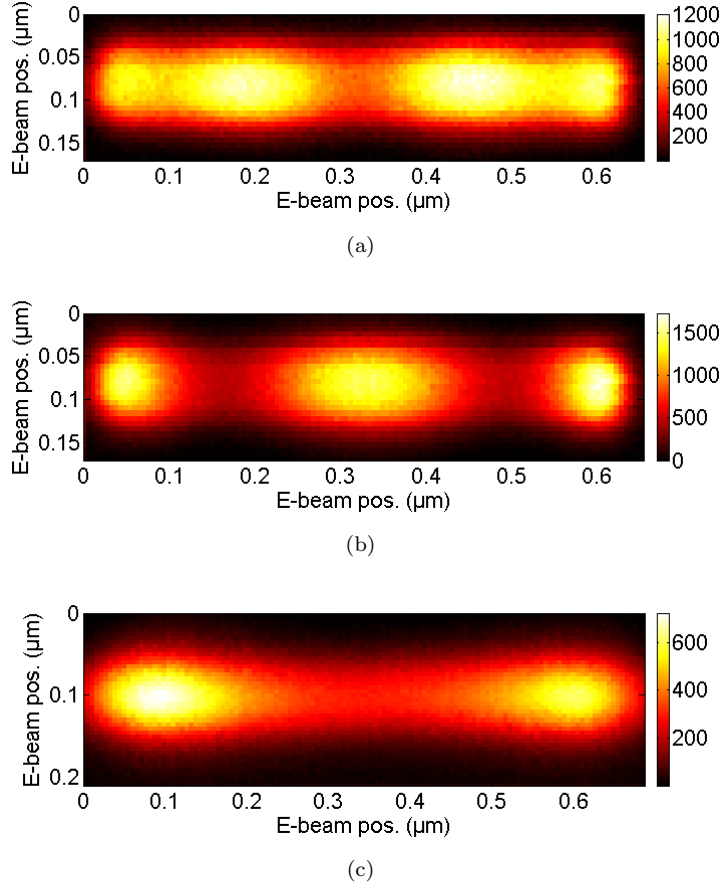
Figure 5.2: Wavelength cross sections of the spectral image showing CL-intensity as function of e-beam position for (a) 600 nm (b) 750 nm and (c) 910nm.

$$\phi = -\frac{\pi(2n'_{spp}W_{res} - m\lambda_0)}{\lambda_0} \qquad (5.2)$$

From Figs. 5.2 and 5.3 it can be seen that the modes are excited effectively at different positions of the wire. The mode at 910 nm is only excited efficiently near the ends of the ridge. The mode at 750 is also effectively excited at the center of the ridge while the mode at 600 nm is excited more efficiently closer to the ends of the ridge. Figure 5.4 shows the CL-spectra collected at specific positions on the wire.

At the center of the ridge (blue curve) the mode at 750 nm clearly dominates the spectrum while in between the center and the end of the ridge (green curve) the mode at 600 nm is dominant. In the spectrum collected at the end of the ridge (red curve) the peaks are equally pronounced which is to be expected since all modes have antinodes on the ends. For 910 nm we see an increase in CL-intensity when moving from the center to the end of the ridge which is consistent with Fig. 5.2(c).
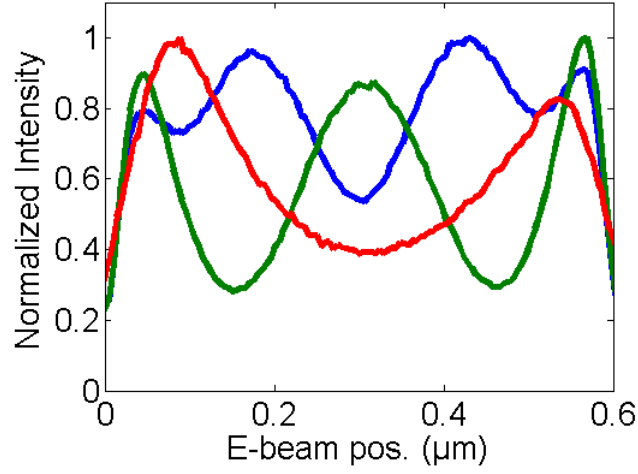
Figure 5.3: Line profiles showing normalized CL-intensity as function of e-beam position along the ridge for 600 nm (blue) 750 nm (green) and 910 nm (red).
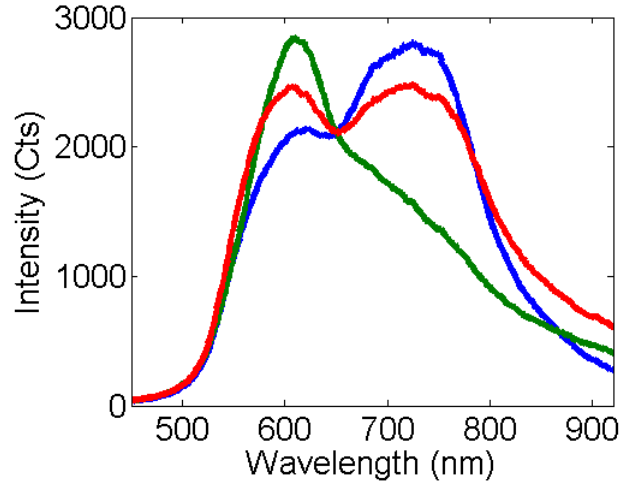
Figure 5.4: Cl-spectra taken at the center of the ridge (blue), at the end of the ridge (red) and in between the center and the end (green)

5.2.2   Angle resolved measurements

Using spatially resolved spectroscopy we have been able to obtain the mode structure for this ridge. This knowledge can be used as input for the angle-resolved measurements.

To resolve the radiation emission pattern as function of excitation position on the ridge, the beam was scanned in a line along the ridge in steps of 10 nm. At every scanning pixel a CCD-image was collected with the 2D CCD-array. Two scans were performed with 40 nm bandpass filters centered at 600 nm and 750 nm respectively, corresponding to the most pronounced modes on the ridge Fig. 5.4. A third scan was done without a color-filter to obtain the radiation pattern integrated over all (visible) wavelengths. The ridge was perpendicularly oriented with respect to the optical axis of the paraboloid.

The raw measurement data was divided by a reference measurement to reduce the effect of the fringes in the image. Unfortunately the fringes moved each measurement due to small displacements of the mirror and SEM-stage, making it impossible to divide them out with only this single reference measurement. In future experiments more reference measurements should be done to effectively correct the data. Figure 5.5 shows $I(\theta, \phi)$ for five positions on the ridge (left end,1/4, center, 3/4 and right end of the ridge) for the three different scans. The hole and the mirror shape can clearly be distinguished.

The gold ridge has axial symmetry and the experimental emission patterns display similar symmetry. There is a slight asymmetry perpendicular to the antenna axis. This is due to the fact that the top part of the emission pattern corresponds to a part of the parabolic mirror that collects a low amount of solid angle and a has numerous small abberations. This creates a large uncertainty in the intensity and makes it difficult to draw any conclusions from this part. Therefore we will focus on the changes in emission pattern, parallel to the ridge axis.

As expected the emission patterns are approximately symmetric when the ridge is excited in the center. Additionally the patterns collected at the ridge-ends look antisymmetric. The effect of the standing wave pattern can also clearly be seen in the scans. For 750 nm patterns 1,3 and 5 correspond to antinodes in the standing wave pattern (Fig. 5.3) resulting in high CL-emission. Patterns 2 and 4 correspond to nodes in the standing wave pattern resulting in lower CL-emission. Although not as clear, it can also be seen that for 600 nm pattern 3 is a bit darker than the others. The emission patterns collected for all wavelengths do not display this behavior because clear nodes or antinodes do not exist when integrating over all wavelengths.

5.2.3   Matching results with theory

Predicting the CL-emission of structures in an exact way is not straightforward in general. BEM-calculations can give an accurate description but these can only be done on relatively simple systems with a high degree of symmetry [5, 11, 15].

A relatively simple way to approximate the emission pattern of the ridge is to assume that it emits light as two interfering points sources with a 600 nm spacing. This assumption implies that the SPPs are tightly bound to the ridge and can only escape at one of the endpoints. The e-beam position determines the relative phase of the two so moving the electron beam will influence the emission pattern. The SPP decay length is approximately 4 μm for 580 nm and the reflection coefficient of the end facets is estimated to be 0.15 [11]. We also include contributions from reflected SPPs. Additionally we can add a phase pickup for the reflection for which we use eq. 5.2. We define the following quantities
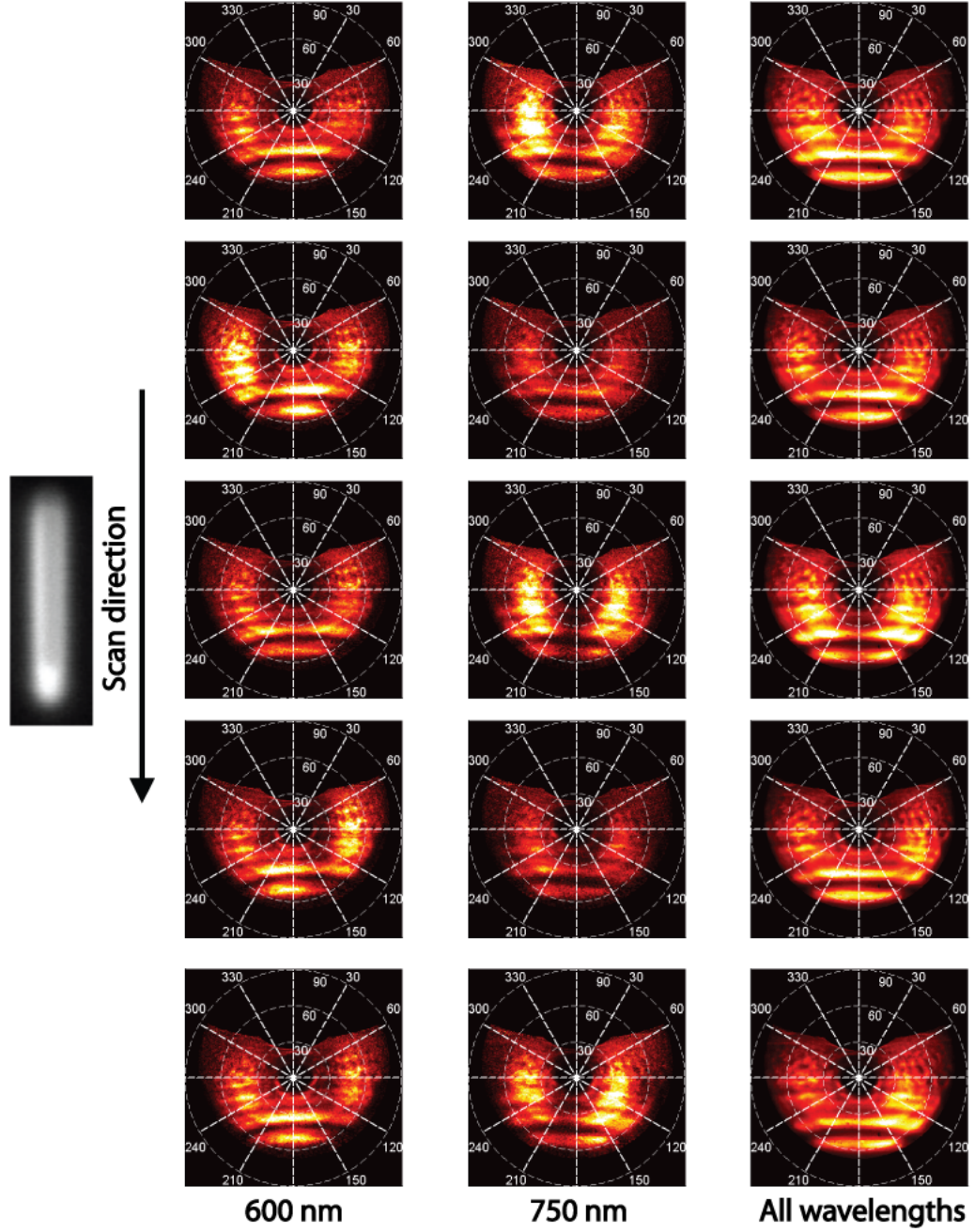
$$n = 0, 1, 2, 3... \tag{5.3a}$$
$$d1_n = 2nL + x_{ebeam} \tag{5.3b}$$
$$d2_n = |(2n+1)L - x_{ebeam}| \tag{5.3c}$$
$$\phi1'_n = d1_n k_{spp} \tag{5.3d}$$
$$\phi2'_n = d2_n k_{spp} + \pi \tag{5.3e}$$

where n is an integer running from zero to infinity which is used to number different SPP

Figure 5.5: I(θ, ϕ) plots for scans performed with 600 nm filter (left) 750 nm filter (center) and without filter (right) for different positions. The scan direction is indicated by the black arrows.

paths. x_{ebeam} is the e-beam position on the wire going from 0 to 600 nm. $d1$ represent the propagation distance of a SPP which couples out at the left end facet of the ridge. After its generation it is either coupled out directly, or it has to reflect $2n$ times and travel $2nL$ before it comes back and is coupled out. $d2$ is the propagation length of plasmons that couple out at the right end facet of the ridge. $\phi1'_n$ and $\phi2'_n$ describes the phase of the SPPs emitted from both ends facets. The extra π in $\phi2'_n$ is added for symmetry reasons.

$$r_1 = \sqrt{x^2 + (y + L/2)^2 + z^2} \tag{5.4a}$$

$$r_2 = \sqrt{x^2 + (y - L/2)^2 + z^2} \tag{5.4b}$$

$$\tag{5.4c}$$

It is assumed that at the ends spherical waves are emitted with a periodicity corresponding to the free space wavelength. r_1 and r_2 describe the position in the spherical waves originating from both ridge ends. Equations 5.5(a,b) describe the spherical waves, taking into account phase pickup, propagation loss and reflection loss.

$$E_1(x, y, z) = \Sigma_{i=0}^{n} \exp[ik_0 r_1 + i\phi1'_n + 2in\phi'_{ref}] \cdot \exp[d1_n/L_{spp}] \cdot r^{2n} \cdot (1 - r) \tag{5.5a}$$

$$E_2(x, y, z) = \Sigma_{i=0}^{n} \exp[ik_0 r_2 + i\phi2'_n + 2in\phi'_{ref}] \cdot \exp[d1_n/L_{spp}] \cdot r^{2n} \cdot (1 - r) \tag{5.5b}$$

$$I_{tot}(x, y, z) = |E_1 + E_2|^2 \tag{5.5c}$$

| (a) | (b) | (c) |

| (d) | (e) | (f) |
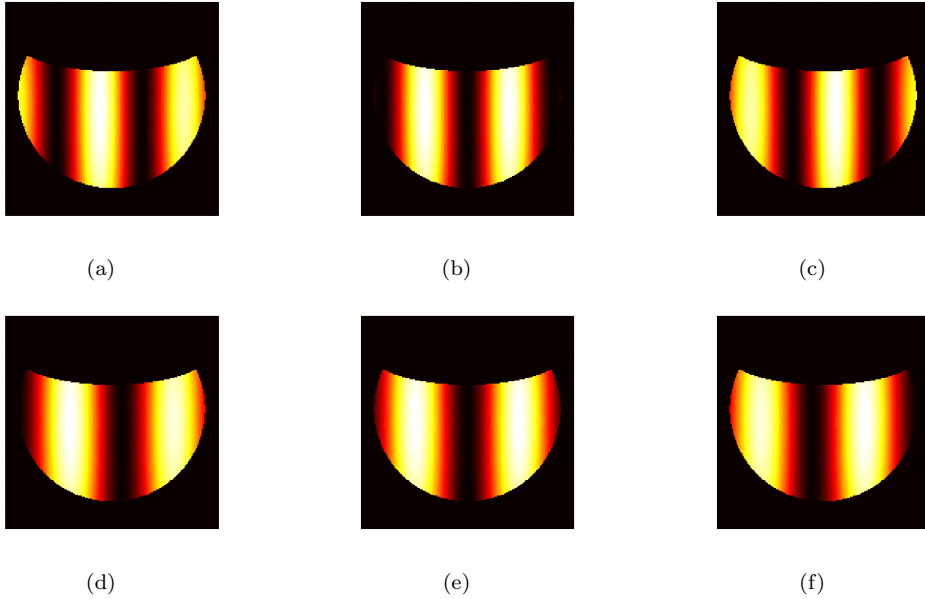
Figure 5.6: Calculated emission intensity as function of θ and ϕ for excitation at (a,d) the left end (b,e) the center and (c,f) the right end of the ridge. Only the angles that are collected by the mirror are shown.

Addition of the two waves gives the total intensity profile in cartesian space. By performing a coordinate transformation we can find I(θ,ϕ) for a particular e-beam position and wavelength. The model does not take into account the intensity variations due to standing wave

patterns on the ridge.

The model predicts bright bands that move when the excitation position is varied. The number of bands present in the model increases with increasing L and k_0. The exact position of the bands depends mainly on x_{ebeam}, L, k_0 and n'_{spp}.

Figure 5.6(a-c) shows calculated emission patterns for excitation at the ends and at the center of the ridge for λ_0=600 nm and $n'_{spp} = 1.3$ (experimentally determined). In (d-f) it is shown for λ_0=750 nm and $n'_{spp} = 1.1$. Only the angles that are collected by the mirror are shown. In the calculations the ridge length was a free parameter and for this particular input L=750 nm gives the best correspondence with experiment.

We can see that these parameters give the right number of peaks for both wavelengths. When the electron beam is in the center the model predicts a dark band in the center which can also be seen in the experimental data. The predicted emission patterns for excitation of the ridge ends seem to be quite similar to the experimental patterns. Note that the predicted patterns at the end points are symmetric with respect to each other and the patterns calculated for center excitation themselves, also show mirror symmetry which is what we expect taking into account the symmetry of the ridge.

5.3   Conclusion

By using spatially resolved CL-spectroscopy we were able resolve the mode structure of a single crystal gold ridge. These results were used as input for angular resolved CL-measurements. By scanning the electron beam it was possible to obtain the emission pattern as function of excitation position.

We applied a simple interference model and found that it predicts radiation bands perpendicular to the main ridge axis which is consistent with the data. The position and number of bands was best reproduced with a ridge length of 750 nm which is 150 nm longer than the physical length, so the description is not entirely accurate. Nevertheless it gives a feeling of what parameters are important in determining the final emission pattern for a certain excitation position.

In a future experiment it might be interesting to study the influence of the ridge on the TR-emission close to the antenna to obtain an idea of how strongly it influences point source emission. Also it would be interesting to repeat this experiment for longer ridges because they can support more Fabry-Pérot resonances it would be possible to see more bands appear as when going to higher resonance orders.

Chapter 6

Local excitation of plasmonic particle array antennas

## 6.1 Introduction

Plasmonic nanoantennas have gained great interest due to their ability to direct the light emission of emitters and their ability to confine light to sub-wavelength volumes [18, 22, 23]. In general the antennas have sub-wavelength dimensions making it impossible with free space light to spatially resolve the physical response with high resolution.

With CL-spectroscopy the excitation resolution is not limited by the diffraction limit of light. Electron beam excitation can be seen as an effective point excitation (10 nm). This point excitation can be regarded as a quasi-single emitter and is useful to study the influence of an nanoantenna on the radiation emission from a point source.

6.2 Experiment

In this experiment we investigate the CL-emission of particle array antennas consisting of five gold nanoparticles fabricated with electron beam lithography on a crystalline silicon substrate. Figure 6.1 shows SEM-micrographs of two particle antennas with similar particle sizes (98 nm and 90 nm) but different pitches of 135 nm and 191 nm respectively.

(a)   (b)
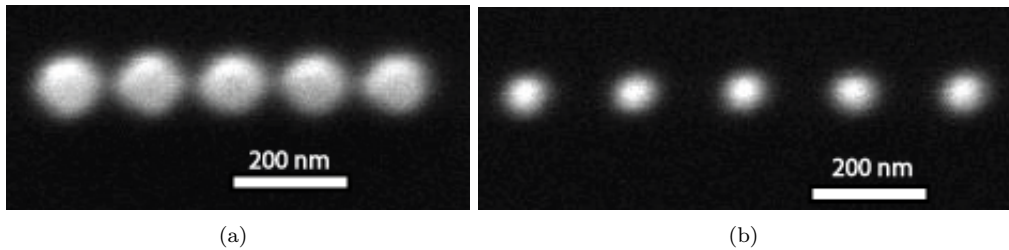
Figure 6.1: SEM-micrographs of gold particle array with (a) small pitch and (b) large pitch.

2D spectral scans with 10 nm spatial resolution were collected for both arrays. Figure 6.2

shows wavelength slices through both spectral scans with a 10 nm bandwidth.
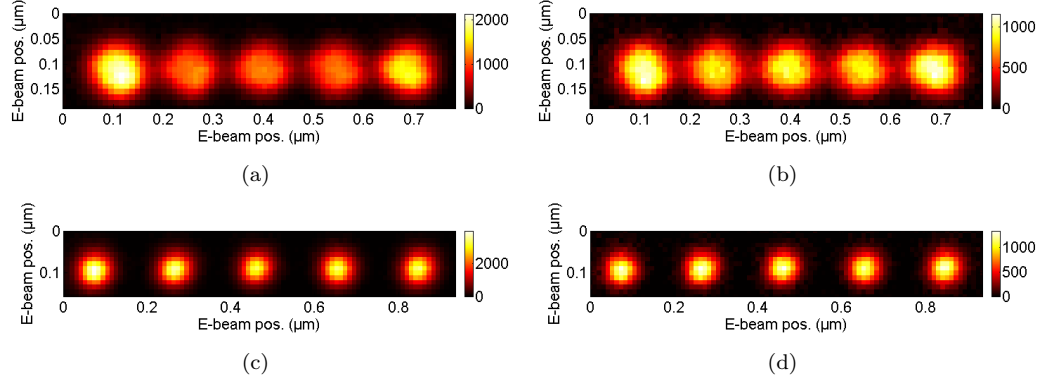
Figure 6.2: Wavelength slices through spectral scans with 10 nm bandwidth, showing CL-intensity (CCD-cts) as function of e-beam position for small pitch array at (a) 600 nm and (b) 700 nm and large pitch array at (c) 600 nm and (d) 700 nm.

The scans are very clear proving that high resolution CL-spectroscopy is a useful tool for characterization and imaging of metal nanoparticles. For the large pitch array, the CL-emission is very similar for each particle. For the small pitch array the two outer particles are more intense. This can be quantified by looking at line cuts through Figs. 6.2(a,b) yielding the line profiles shown in Fig. 6.3.

The relative variations between the outer and inner dots are significant for the small pitch array while the variations for the large pitch array are much smaller and seem to be random. Figure 6.4 shows absolute CL-spectra for each dot in both arrays. The broad silicon background was subtracted to solely show the nanoparticle emission.

In Fig. 6.4(a) the difference between the inner and outer dots is clearly visible for the small pitch array. For the large pitch array the variations are small and the spectra appear very similar.

In the fabrication of nanoparticles there are always small stochastic variations in size. Since the electric polarizability of a metal particle is proportional to particle volume, a small variation in radius can lead to a substantial difference in polarizability. Therefore particles with a slightly larger radius can generate significantly more CL-emission. In EBL, particles can also vary in size due to proximity effects in the resist. However, this effect would yield larger particles in the center and smaller particles at the end in which case we should see high CL-intensity from the inner particles and low CL-intensity from the outer particles. As shown in Figs.2-4 the opposite behavior is observed.

A change in size would also shift the resonance-frequency of the particle resulting in a different CL-spectrum. In Fig. 6.4(a) the CL-spectrum for dot 1 has a slightly different shape than the other four. The peak has blue shifted slightly which is not expected for a larger particle. Another possible explanation could be that the particle has a slightly different shape altering the plasmon resonance. Dot 5 does not display a clear spectral shift but still generates ∼1.5 times more CL than the three center particles. This suggests that there is possibly another effect that plays an important role here.
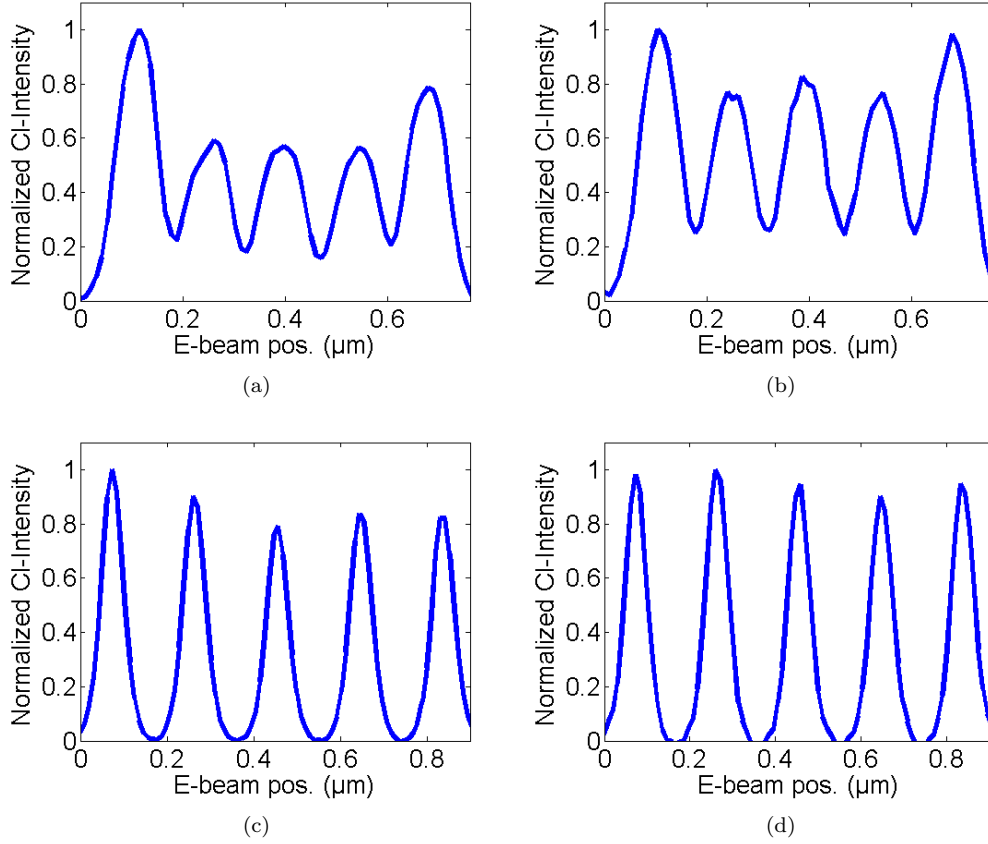
Figure 6.3: CL linecuts of 10 nm bandwidth through the particle arrays showing normalized CL-intensity as function of e-beam position. (a,b) Line cuts through array with small pitch for 600 nm and 700 nm. (c,d) Line cuts through array with large pitch for 600 nm and 700 nm.

The particles in the array are very closely spaced (the gaps are only 40 nm) so there is interaction between the particles. Therefore exciting one particle will induce dipole moments in all the other particles giving rise to interference effects [22, 23]. The outer particles obviously are in a different photonic environment since they only have one nearest neighbor.

The substrate is also important for the behavior of this system. This experiment was performed on silicon which is very suitable for CL-experiments due to its robustness, good conductivity and relatively low background signal. Silicon does have a high refractive index of 3.5. Multiplying the pitch by n gives 459 nm, implying that this particle antenna can act as a grating for visible light. Furthermore, as a result of the high refractive index, a large portion of the CL will be drawn into the substrate. Here it cannot be collected by the parabolic mirror.

All of the effects mentioned above possibly have an influence on the CL-emission pattern and intensity of this particle antenna.
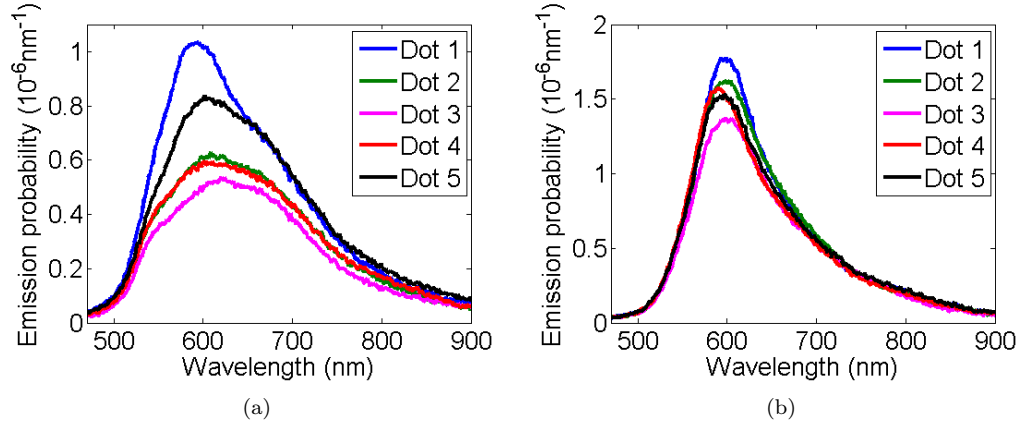
Figure 6.4: CL-spectra showing intensity (CCD-cts) as function of wavelength for each of the dots in the array with small pitch (a) and with large pitch (b) where dot 1 is the outer left dot and dot 5 is the outer right dot.

6.2.1   Angular emission pattern of a particle array antenna

To further explore the physical properties of the small pitch particle array antenna, the emission pattern was measured as function of excitation position. 2D CCD-images were collected for point excitation of each of the particles, yielding five radiation patterns. The integration time per position was 25 seconds. To study the wavelength dependence of the emission 40 nm bandpass filters centered at 400, 500, 600, 650, 700 and 750 nm were used. The images were corrected for dark counts.

Two different types of response were observed. Above 650 nm the emission pattern of the antenna does not depend on which particle is excited. Figure 6.5(a) shows Cl-intensity as function of θ and ϕ for dot 2 measured at 700 nm. It seems that at this wavelength the
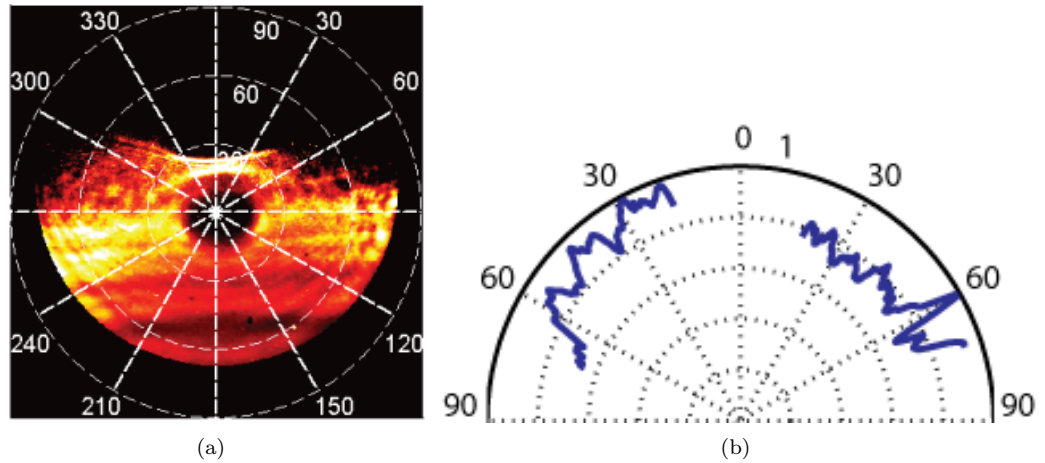
Figure 6.5: (a) CL-intensity at 700 nm ± 20 nm as function θ and ϕ for a particle array nanoantenna excited at dot 2(b) Cross cut of (a) along the main axis of the antenna which gives CL-intensity as function of θ.
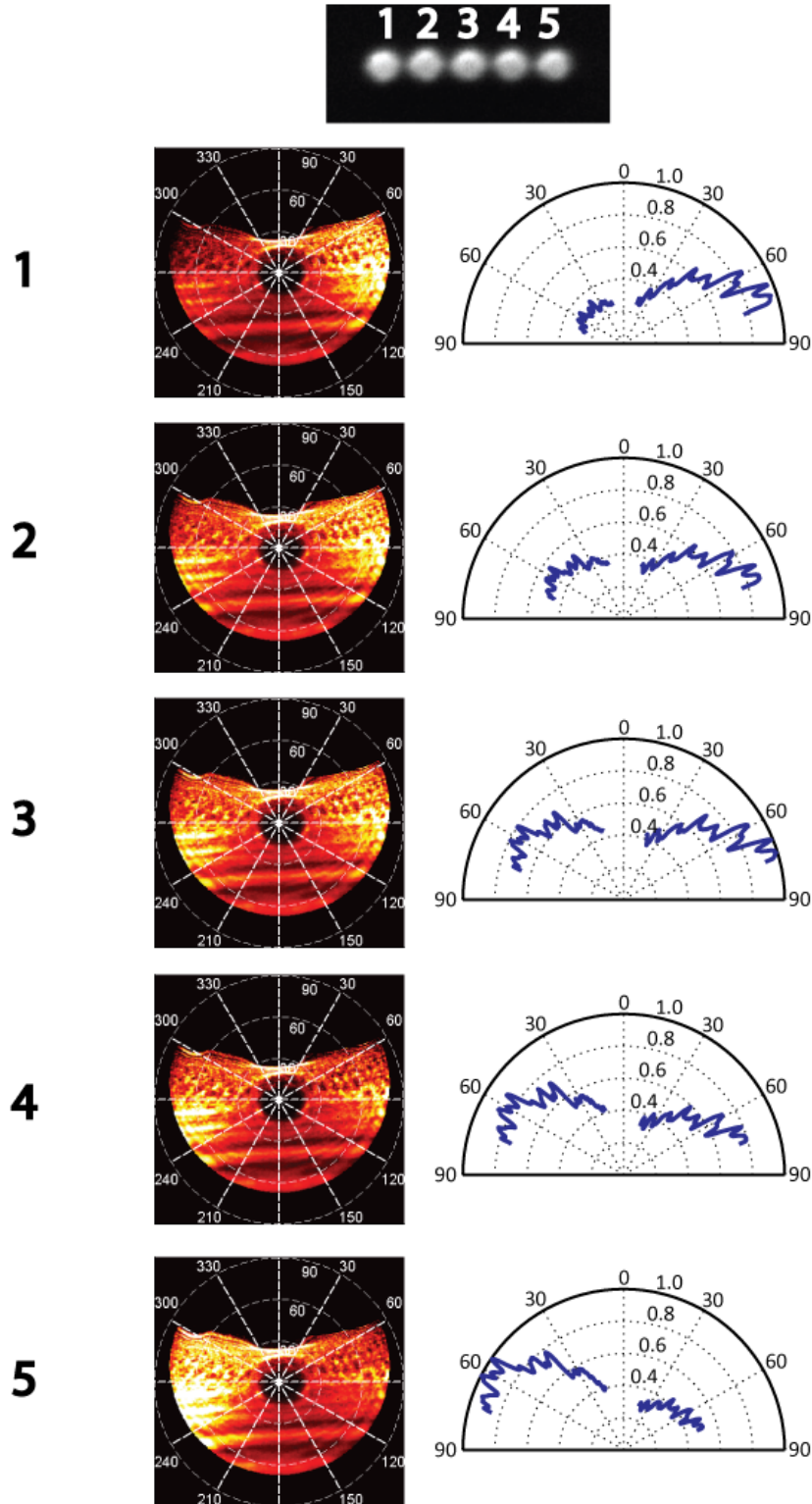
Figure 6.6: On the left CL-intensity as function of θ and ϕ collected with 500 nm filter for each particle is shown. The number corresponds to which particle is excited. On the right cross cuts through the theta phi maps along the main antenna axis giving CL-intensity as function of theta are shown. The intensity is normalized to the maximum CL-intensity.

antenna emits light in a bright band parallel to the array. The patterns observed at 650 nm and 750 nm look very similar.

The emission pattern in Fig. 6.5 shows severe distortions due to the mirror. Nonetheless we can clearly see the trends. The emission pattern clearly has vertical mirror symmetry consistent with the symmetry of the antenna. However, from the antenna geometry we also expect horizontal mirror symmetry and this is not observed. This is due to the fact that the top part of the emission pattern corresponds to a part of the parabolic mirror that collects a low amount of solid angle and a has numerous small abberations. This creates a large uncertainty in the intensity and makes it difficult to draw any conclusions from this area. Therefore we will focus on the changes in emission pattern, parallel to the antenna axis.

To clarify the radiation emission along the antenna axis a cross cut of ten pixels wide was made through (a) which after integration yields the polar plot shown in (b). The hole is located at $\theta = 0$ which is why the intensity was not measured there. Also for $\theta > \sim 75^o$ the intensity was not measured because the mirror does not extend any further. In reality the emission pattern is probably extended below the mirror. The observed emission band resembles a toroid out of the plane of the substrate. This is consistent with a dipole moment in the plane of the substrate perpendicular to the antenna. If the charge oscillations in the the particles would be in phase for this wavelength range this could produce a net dipole moment in this particular direction.

Below 650 nm the antenna displays different behavior. Figure. 6.6 shows the angular emission patterns collected for each particle for 500 nm. Furthermore cross cuts through the $I(\theta, \phi)$-plots along the main antenna axis are shown yielding polar plots which show CL-intensity as function of θ.

It is obvious that the excitation position does play an important role now in the emission pattern of the antenna. The antenna clearly seems to direct the radiation in a beam. When exciting particles 1 and 5 the radiation is mainly directed along the antenna. Particles 2 and 4 each have one neighbor on one side and three on the other. Most of the radiation is still directed towards the largest particle number but the effect is not as significant as
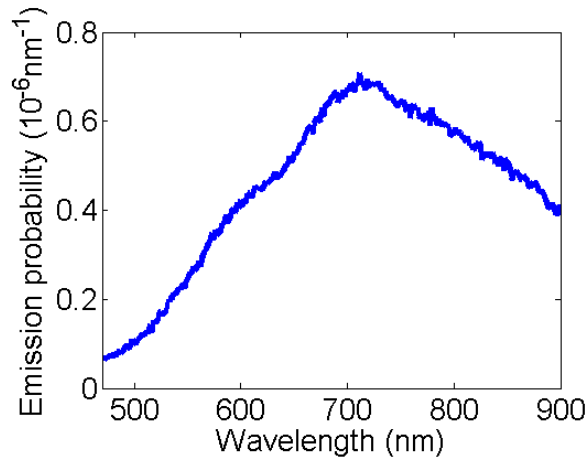
Figure 6.7: CL-intensity as function of wavelength for the silicon substrate for 30 keV electron excitation.

for particles 1 and 2. As expected, the emission pattern is approximately symmetric for particle 3 which has an equal amount of neighbors on both sides. Comparing with Fig. 6.5 it is clear that below 650 nm most of the radiation is emitted under shallower angles. The CL-emission is distributed over a larger range of ϕ.

With an emission probability of only $0.95 \cdot 10^{-7}/\text{nm}/e^-$, the amount of CL at 500 nm is relatively small for the gold particles (see Fig. 6.4) compared to other wavelengths. Figure 6.7 shows a CL-spectrum of the silicon background. At 500 nm the emission probability is $1.02 \cdot 10^{-7}/\text{nm}/e^-$ so a significant fraction of the CL-emission originates from the silicon substrate in this wavelength range.

We can conclude from this, that perhaps not only the plasmonic CL-emission from the particle but also light emission coming from the substrate is directed by the antenna.

6.3   Conclusion

We have shown that a gold nanoparticle array antenna on silicon can direct CL-emission below 650 nm. In this wavelength range the emission pattern clearly depends on the excitation position. Since the e-beam is a quasi point source, this experiment provides insight into how the radiation of single emitters can be directed.

Due to the high index substrate, a significant ampount of the CL will be radiated into the subtrate. Lowering the index of the substrate would reduce this effect, but most low index substrates are incompatible with CL-Spectroscopy due to charging effects and/or high background signal. Specially designed geometries fabricated with FIB-milling of a MIM stack for instance, might provide an outcome.

Chapter 7

Fabry-Pérot plasmon resonances in a silver wedge antenna

7.1 Introduction

It has been shown in the past that metallic nanowires or nanostructured grooves in a metal substrate can act as organ pipe resonators for visible light [19, 20, 24] amplifying wavelengths that exactly fit into the resonator.

In this experiment we study the resonant behavior of high aspect-ratio silver wedge antennas using high resolution spatially resolved CL-spectroscopy. These antennas support transverse Fabry-Pérot plasmon resonances. Since the width is not fixed in such a wedge there are resonances for a large range of wavelengths.

7.2 Experimental

Silver wedge antennas of 20 nm thickness were fabricated on a silicon on insulator (SOI) substrate consisting of a 40 nm Si layer with 400 nm buried SiO_2 below and a 20 nm thick SiO_2 layer on top, using e-beam lithography. The antennas were covered with a 5 nm thick alumina layer using atomic layer deposition (ALD) to prevent oxidation of the silver. The wedges are 65 μm long and up to 4 μm wide. The opening angle of the wedges is so small (1.75°) that the sidewalls can be regarded as being effectively parallel. Figure 7.1 shows a schematic drawing and a SEM micrograph of the structure.

The advantage of using this particular substrate is that the 20 nm SiO_2 layer gives it a substantially lower effective refractive index than a pure silicon substrate, while the silicon layer still prevents charging effects. A disadvantage is the substantial background level due to defect luminescence in the SiO_2 and Al_2O_3.

For simplicity, we will disregard the alumina and the silicon layer in the following discussion. The metal film then has an asymmetric dielectric environment with a glass substrate below and air on top. There are two distinct modes that can be excited on the silver film. A symmetric mode which is not tightly bound to the film, can be excited on the low index side (air side) of the film. This mode cannot be confined effectively to the narrower part of the wedge because the radiation losses due to far field coupling become too high. On the high index side (glass side) of the film, a tightly bound short-range (SR) SPP mode can be

(a)

(b)
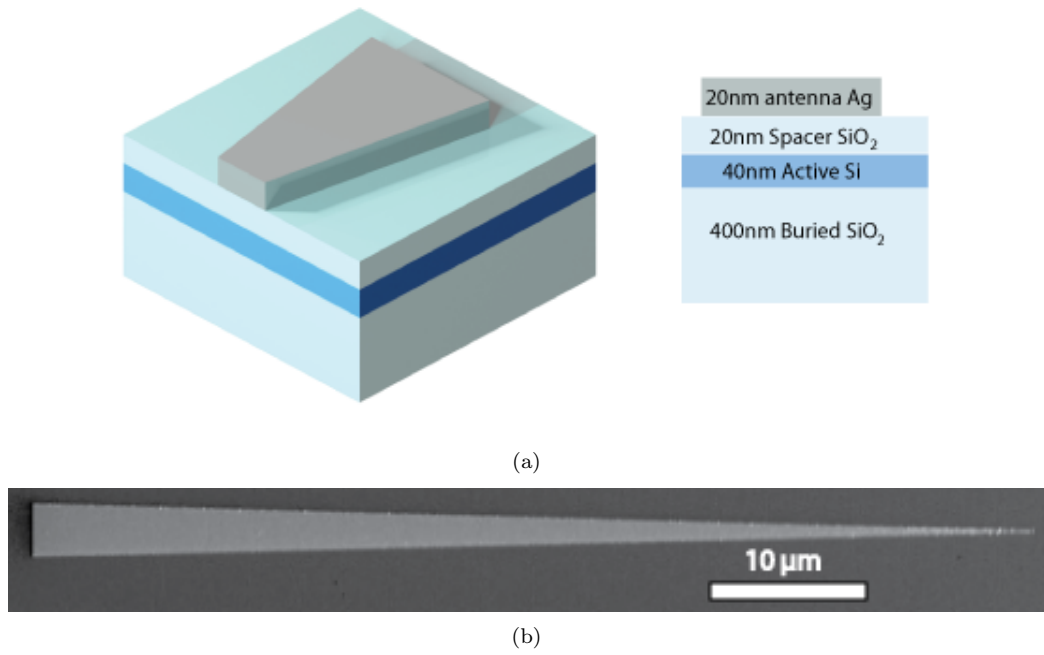
Figure 7.1: (a) 3D representation of the wedge antenna together with a cross section showing the thicknesses of the different layers. (b) SEM micrograph of a silver wedge antenna.

excited [25–27] which theoretically does not have any radiation losses except at the sidewalls of resonator. This bound SPP mode is transverse magnetic (TM) and has an asymmetric electric field profile as shown in Fig. 7.2. It is this SR-SPP mode that should show strong Fabry-Pérot resonances for which we can use CL-spectroscopy to resolve their spatial profile [19, 20].

Figure 7.3(a) shows dispersion relations for both modes [26] using calculated tabulated optical constants [28]. It is clear that the asymmetric mode has a significantly higher mode index (2.45 compared to 1.03 for λ=700 nm) confirming that light is indeed confined more strongly. In Fig. 7.3(b) calculated propagations lengths as function of wavelength are shown for the two modes. We can see that in the visible range of the spectrum the propagation lengths are short for the asymmetric mode. There is strong Ohmic damping in this wavelength range so short propagation lengths are expected.
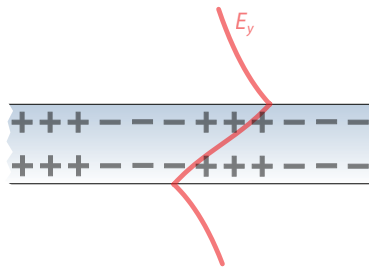
Figure 7.2: Electric field profile for the asymmetric bound mode on a thin silver film.
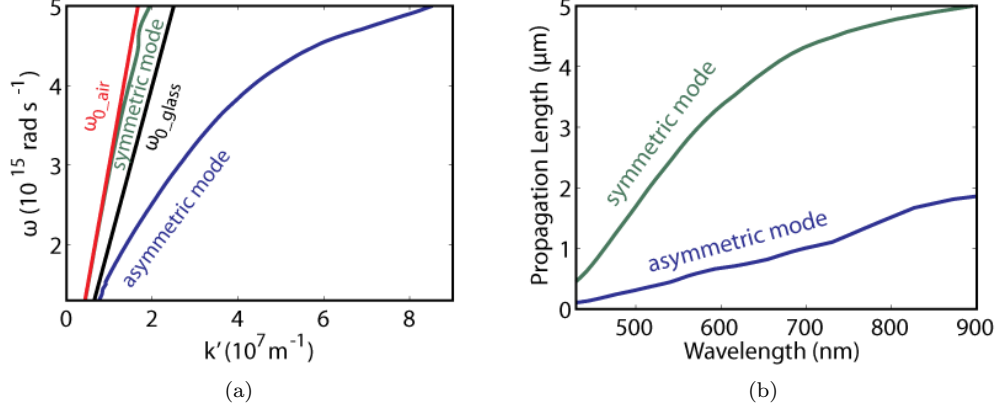
Figure 7.3: (a) Dispersion relations for the symmetric and antisymmetric plasmon modes. The light lines in glass and air are also included. (b) Propagation length as function of wavelength for the different modes.

The wegdes are several tens of microns long and the propagation length of SPPs in the visible range of the spectrum is in the order of $1 \ \mu m$ (see Fig. 7.3(b)). As a result there can only be transverse Fabry-Pérot plasmon resonances. The resonance condition is given by

$$W_{res,m} = \frac{m - \phi/\pi}{2} \cdot \frac{\lambda_0}{n'_{spp}} \qquad (7.1)$$

where $W_{res,m}$ is the resonator width, m is the resonance order, ϕ is the phase pickup experienced upon reflection, λ_0 is the free space wavelength and n'_{spp} is the mode index [21]. For a fixed wavelength there can be resonances at multiple resonator widths. These resonances should approximately be equally spaced along the antenna. This is schematically illustrated in Fig. 7.4(a). Note that the resonance widths in general are not entirely equal to a multiple integer of $\lambda_{spp}/2$ due to the reflection phase shifts. The reflection phase shifts in this system are close to $\pi/2$ and as a result there can be a significant discrepancy for the lowest order resonances (m=1,2). The resonance widths for these modes can be substantially smaller than $\lambda_{spp}/2$ and λ_{spp}. Because of symmetry reasons it is impossible to excite even modes with light under normal incidence but with an electron beam these modes can be excited as we will show.

To characterize the resonant behavior of the antennas the e-beam was raster scanned over an area in 10 nm steps. At each scanning pixel a CL-spectrum was collected with the CCD. For all stripe widths, a modulation of the CL-intensity across the stripe width with a period of $\sim \lambda_{spp}$ was observed. The intensity of these modulations was constant for all strip widths. This modulation is probably caused by interference of the SR-SPPs which are coupled to the far field from the sidewalls of the wedge, with the TR-radiation which is emitted directly from the excitation position [12].

From the propagation length calculations it is clear that for larger widths there cannot be a significant Fabry-Pérot resonance caused by plasmon-plasmon interference because the losses are simply too high. Therefore we focused on the narrower part of the antennas ($W < 1\mu m$). Figure 7.4(b) shows a wavelength slice through the 2D-spectral image for λ=700 nm. The image was compressed along the antenna axis to clarify the intensity changes in the trans-
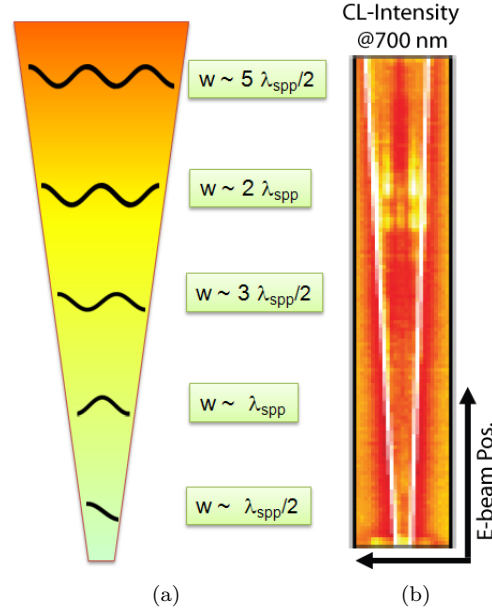
Figure 7.4: (a) Schematic representation of different order resonances corresponding to different widths of the wedge. (b) Wavelength slice through 2D spectral image at 700 nm of narrow part of the wedge.

verse direction. The intensity for some widths is clearly higher than for others suggesting that there are resonances.

If we sum the CL-signal along the minor axis of the antenna and correct for the resonator width we should see a maximum in the integrated CL-intensity when the resonance condition is matched. Figure 7.5 shows the CL-intensity as function of resonator width and wavelength. The black lines indicate where a resonance is expected using eq. 7.1 where n'_{spp} was taken from the dispersion data shown in Fig. 7.3(a) and ϕ was calculated using full-field simulations [21].

Clear diagonal bands can be distinguished corresponding to different order modes. As expected the the resonances shift to larger widths for longer wavelengths. Below 550 nm we do not observe any structure. At these wavelengths the plasmon propagation lengths are extremely short (Fig. 7.3(b)) so there cannot be any plasmon interference. There still should be significant transition radiation emission which is independent of e-beam position on the antenna. This possibly explains the bright band. Additionally, discrete steps in the resonance bands can be observed. Because of the EBL fabrication process the increase in width of the wedges is incremental instead of continuous resulting in a stepwise dataset.

Since the scans were performed with 10 nm spatial resolution it is possible to resolve the standing wave patterns for different order resonances. On the left of Fig. 7.6 CL-intensity as function of wavelength and e-beam position along the transverse direction of the wedge is shown for different resonator widths. On the right line cuts through the intensity maps are shown for $\lambda = 700$ nm. Note that the background has been subtracted from these plots. Because the silver film blocks a part of the background radiation the overall CL-intensity measured on the film is actually lower than next to the film yielding negative intensity on the film. This effect is most pronounced in the center of the antenna which is why the
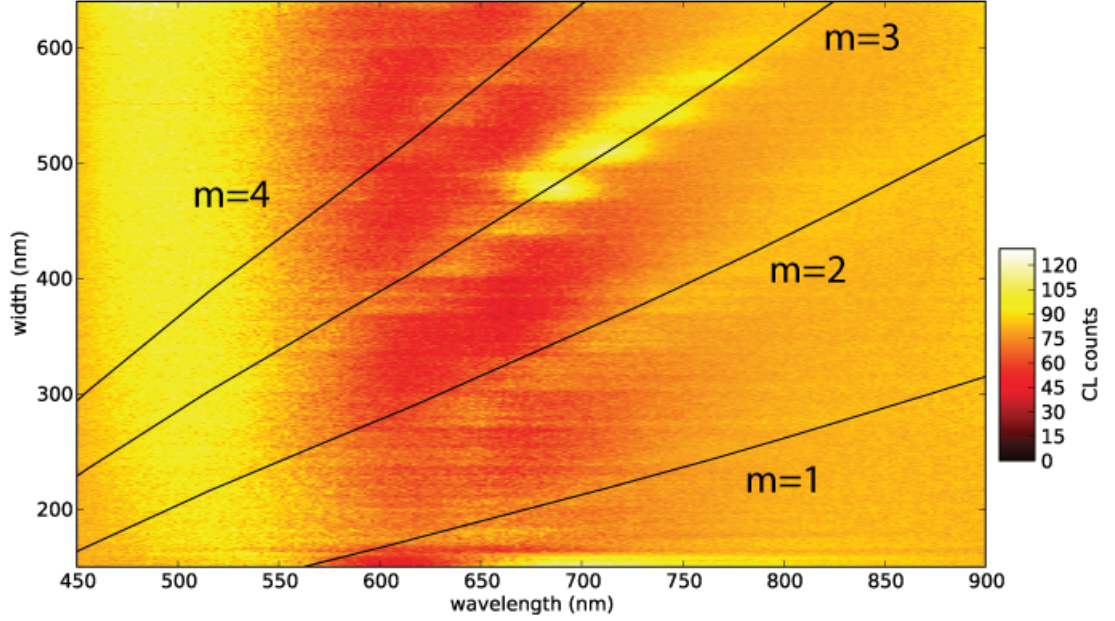
Figure 7.5: CL-intensity as function of resonator width and wavelength. The black lines show where a resonance is expected for different resonance orders using the Fabry-Pérot model. A $m=5$ band is also still vaguely visible on the top left of the figure.

CL-intensity is so low in the center for the line cuts showing the $m=3$, $m=4$ and $m=5$ mode.

These plots confirm that we are dealing with different order resonances. As expected we see 3,4,5 and 6 peaks for $m=2$, $m=3$, $m=4$ and $m=5$ respectively. If we look at the wavelength versus e-beam position for $W=630$ nm we can also vaguely see an $m=6$ interference pattern with seven peaks at ∼630 nm. Although it is not shown here, we have also observed a two peak standing wave pattern corresponding to the $m=1$ mode (it is present in Fig 7.5). Since we clearly see the interference pattern for $m=2$ and $m=4$ we can conclude that the electron beam can indeed couple to even number modes effectively. The peak spacing in these standing patterns should correspond to $\lambda_{spp}/2$. We find a peak spacing of approximately 140 nm which corresponds to a $n'_{spp}=2.5$ which is close to the calculated mode index for 700 nm.

To confirm that the observed behavior can truly be attributed to the plasmon mode discussed above we checked that the resonances are caused by a TM-mode. We repeated the measurement of which the result is shown in Fig.7.5 with polarization sensitive detection (see chapter 2). The polarizer was calibrated using the TR-signal from a gold pad which was also present on the sample. Subsequently two scans were performed for both horizontal and vertical orientation of the wedge. In the scan for the vertical orientation which should correspond to an emission polarization perpendicular to the stripe, the resonant behavior is clearly visible while for the horizontal orientation which should correspond to an emission polarization along the stripe it is not. This result is consistent with what we expect for a TM-mode.

7.3   Conclusion

We have used spatially resolved CL-spectroscopy to resolve the transverse Fabry-Pérot resonances in a silver wedge antenna. We have shown that the resonant behavior can be explained with a simple Fabry-Pérot model which includes the reflection phase shift. Furthermore we have been able to resolve the spatial profiles of higher order modes up to $m=6$. In the near future we will try to match these results with photocurrent measurements performed on the same samples.
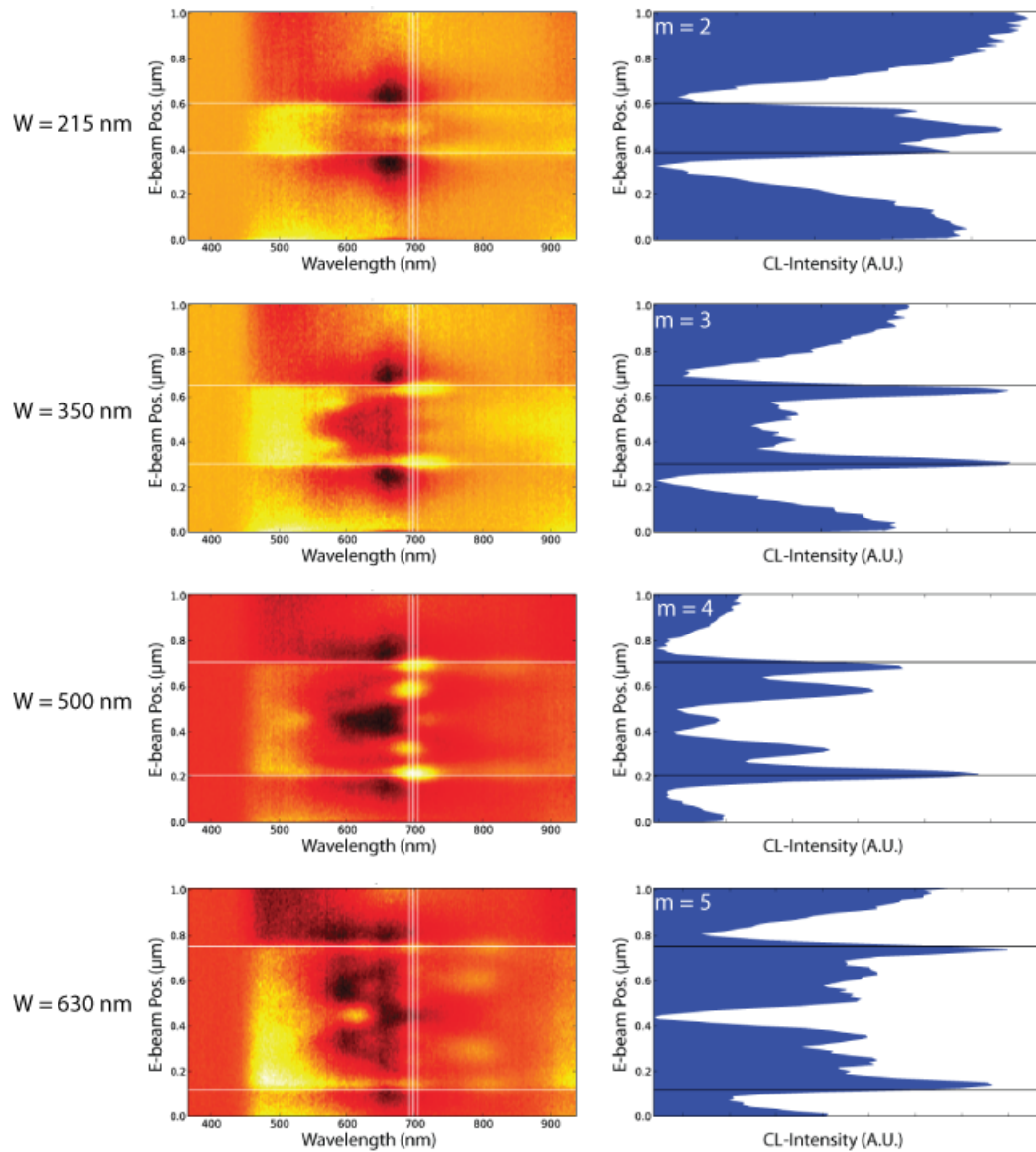
Figure 7.6: Left panels: CL-intensity as function of e-beam position and wavelength for different resonator widths. The white horizontal lines mark the sidewalls of the wegde. The central vertical line indicates the center wavelength (700 nm) of the line cut (Right panels) and the outer lines indicate the spectral integration bandwidth (17 nm). On the top left of each line cut plot the mode number corresponding to the interference pattern is given.

Bibliography

[1] H. A. Atwater and A. Polman, *Plasmonics for improved photovoltaic devices*, Nature Materials **9**, 205 (2010).

[2] S. P. Burgos, R. de Waele, A. Polman, and H. A. Atwater, *A single-layer wide-angle negative index metamaterial at visible frequencies*, Nature Materials **9**, 407 (2010).

[3] A. Polman, *Plasmonics applied*, Science **322**, 868 (2008).

[4] F. J. García de Abajo, *Optical excitations in electron microscopy*, Reviews of Modern Physics **82**, 209275 (2010).

[5] M. Kuttge, *Cathodoluminescence plasmon microscopy*, PhD thesis, AMOLF, 2009.

[6] T. van Wijngaarden, *Cathodoluminescence Imaging Spectroscopy on Plamonic Structures*, Master's thesis, AMOLF, 2005.

[7] G. E. Lloyd, *Atomic number and crystallographic contrast images with the SEM: a review of backscattered electron techniques*, Mineralogical Magazine **51**, 319 (1987).

[8] J. Prangsma, *Local and dynamic properties of light interacting with subwavelength holes*, PhD thesis, AMOLF, 2009.

[9] P. B. Johnson and R. W. Christy, *Optical Constants of the Noble Metals*, Physical Review Letters B **6**, 43704379 (1972).

[10] H. Raether, *Surface Plasmons on Smooth and Rough Surfaces and on Gratings*, Springer, 1988.

[11] E. J. R. Vesseur, R. de Waele, H. J. Lezec, H. A. Atwater, F. J. García de Abajo, and A. Polman, *Surface plasmon polariton modes in a single-crystal Au nanoresonator fabricated using focused-ion-beam milling*, Applied Physics Letters **92**, 83110 (2008).

[12] M. Kuttge, E. J. R. Vesseur, A. F. Koenderink, H. J. Lezec, H. A. Atwater, F. J. García de Abajo, and A. Polman, *Local density of states, spectrum, and far-field interference of surface plasmon polaritons probed by cathodoluminescence*, Physical Review Letters B **79**, 113405 (2009).

[13] M. Kuttge, E. J. R. Vesseur, J. Verhoeven, H. J. Lezec, H. A. Atwater, and A. Polman, *Loss mechanisms of surface plasmon polaritons on gold probed by cathodoluminescence imaging spectroscopy*, Applied Physics Letters **93**, 113110 (2008).

[14] J. van Wijngaarden, E. Verhagen, A. Polman, C. Ross, H. J. Lezec, and H. A. Atwater, *Direct imaging of propagation and damping of near-resonance surface plasmon polaritons using cathodoluminescence spectroscopy*, Applied Physics Letters **88**, 221111 (2006).

[15] E. J. R. Vesseur, F. J. García de Abajo, and A. Polman, *Modal decomposition of surface-plasmon whispering gallery resonators*, Nano Letters **9**, 3147 (2009).

[16] G. Vecchi, V. Giannini, and J. Gómez Rivas, *Shaping the Fluorescent Emission by Lattice Resonances in Plasmonic Crystals of Nanoantennas*, Physical Review Letters B **102**, 146807 (2009).

[17] O. L. Muskens, V. Giannini, J. A. Sánchez-Gil, and J. Gómez Rivas, *Strong Enhancement of the Radiative Decay Rate of Emitters by Single Plasmonic Nanoantennas*, Nano Letters **7**, 28712875 (2007).

[18] T. H. Taminiau, F. D. Stefani, F. B. Segerink, and N. F. van Hulst, *Optical antennas direct single-molecule emission*, Nature Photonics **2**, 234237 (2008).

[19] M. Kuttge, E. J. R. Vesseur, and A. Polman, *Fabry-Pérot resonators for surface plasmon polaritons probed by cathodoluminescence*, Applied Physics Letters **94**, 183104 (2009).

[20] E. J. R. Vesseur, R. de Waele, M. Kuttge, and A. Polman, *Direct observation of plasmonic modes in*

Au nanowires using high-resolution cathodoluminescence spectroscopy, Nano Letters **7**, 2843 (2007).

[21] E. S. Barnard, J. S. White, A. Chandran, and M. L. Brongersma, *Spectral properties of plasmonic resonator antennas*, Optics Express **16**, 16529 (2008).

[22] A. F. Koenderink, *Plasmon Nanoparticle Array Waveguides for Single Photon and Single Plasmon Sources*, Nano Letters **9**, 42284233 (2009).

[23] R. de Waele, A. F. Koenderink, and A. Polman, *Tunable Nanoscale Localization of Energy on Plasmon Particle Arrays*, Nano Letters **7**, 2004 (2007).

[24] H. Ditlbacher, A. Hohenau, D. Wagner, U. Kreibig, M. Rogers, F. Hofer, F. R. Aussenegg, and J. R. Krenn, *Silver Nanowires as Surface Plasmon Resonators*, Physical Review Letters B **95**, 257403 (2005).

[25] E. Verhagen, A. Polman, and L. Kuipers, *Nanofocussing in laterally tapered plasmonic waveguides*, Optics Express **16**, 45 (2008).

[26] E. Verhagen, *Subwavelength light confinement with surface plasmon polaritons*, PhD thesis, AMOLF, 2009.

[27] E. N. Economou, *Surface Plasmons in Thin Films*, Physical Review Letters **182**, 539 (1969).

[28] E. D. Palik, *Handbook of Optical Constants*, Academic Press, New York, 1985.

Acknowledgements